

Seasonal Mixed Layer Temperature in the Congolese Upwelling System

Key Points:

- Balance between incoming shortwave radiation inducing heating and vertical mixing at the base of the mixed layer inducing cooling in the Congolese upwelling system
- Seasonal cooling due to the combined effect of vertical advection by equatorially-forced upwelling, coastally-trapped waves and shallow vertical mixing

R. D. Ngakala^{1,2} , G. Alory³ , C. Y. Da-Allada^{1,4,5}, I. Dadou³, C. Cardot³, G. Morvan³, J. Jouanno³ , S. Illig^{3,6} , and E. Baloïtcha¹

¹Department of Oceanography and Applications, International Chair in Mathematical Physics and Applications, University of Abomey-Calavi, Cotonou, Benin, ²Department of Oceanography and Environment, Institut National de Recherche en Sciences Exactes et Naturelles, Pointe-Noire, Republic of the Congo, ³Université de Toulouse, LEGOS (CNES/CNRS/IRD/UPS), Toulouse, France, ⁴Laboratoire de Géosciences, de l'Environnement et Applications, Université Nationale des Sciences Technologies, Ingénierie et Mathématiques, Abomey, Benin, ⁵Laboratoire d'Hydrologie Marine et Côtière, Institut de Recherches Halieutiques et Océanologiques du Bénin, Cotonou, Benin, ⁶Department of Oceanography, University of Cape Town, Rondebosch, South Africa

Supporting Information:

Supporting Information may be found in the online version of this article.

Correspondence to:

R. D. Ngakala,
roy.ngakala@gmail.com

Citation:

Ngakala, R. D., Alory, G., Da-Allada, C. Y., Dadou, I., Cardot, C., Morvan, G., et al. (2025). Seasonal mixed layer temperature in the Congolese upwelling system. *Journal of Geophysical Research: Oceans*, 130, e2023JC020528. <https://doi.org/10.1029/2023JC020528>

Received 5 OCT 2023
Accepted 30 DEC 2024

Author Contributions:

Conceptualization: R. D. Ngakala, G. Alory
Data curation: G. Morvan, J. Jouanno
Formal analysis: R. D. Ngakala, C. Cardot
Investigation: R. D. Ngakala
Methodology: R. D. Ngakala, G. Alory, C. Y. Da-Allada
Resources: G. Morvan, J. Jouanno
Supervision: G. Alory, C. Y. Da-Allada, I. Dadou
Visualization: R. D. Ngakala
Writing – original draft: R. D. Ngakala
Writing – review & editing: R. D. Ngakala, G. Alory, C. Y. Da-Allada, I. Dadou, C. Cardot, G. Morvan, J. Jouanno, S. Illig, E. Baloïtcha

Abstract The Congolese upwelling system (CoUS), located along the West African coast north of the Congo River, is one of the most productive and least studied systems in the Gulf of Guinea. The minimum sea surface temperature in the CoUS occurs in austral winter, when the winds are weak and not particularly favorable to coastal upwelling. Here, for the first time, we use a high-resolution regional ocean model to identify the key atmospheric and oceanic processes that control the seasonal evolution of the mixed layer temperature in a 1°-wide coastal band from 6°S to 4°S. The model is in good agreement with observations on seasonal timescales, and in particular, it realistically reproduces the signature of the surface upwelling during the austral winter, the shallow mixed layer due to salinity stratification, and the signature of coastal wave propagation. The analysis of the mixed layer heat budget for the year 2016 reveals a competition between warming by air-sea fluxes, dominated by the incoming shortwave radiation throughout the year, and cooling by vertical mixing at the base of the mixed layer, as other tendency terms remain weak. The seasonal cooling is induced by vertical mixing, where local wind-driven dynamics play a secondary role compared to subsurface processes. A subsurface analysis shows that remotely forced coastal-trapped waves raise the thermocline from April to August, which strengthens the vertical temperature gradient at the base of the mixed layer and leads to the mixing-induced seasonal cooling in the Congolese upwelling system.

Plain Language Summary The Congolese upwelling system is located along the West African coast north of the Congo River. It is one of the most productive systems in the Gulf of Guinea but has received little attention due to the lack of historical data in this coastal region. Low temperatures occur during the austral winter when winds are weak in the area. We use a high-resolution regional ocean model to identify the main atmospheric and oceanic forcing controlling the seasonal changes in sea surface temperature. We find a competition between warming by air-sea fluxes, dominated by the incoming shortwave radiation throughout the year, and cooling by vertical mixing. The seasonal occurrence of low temperature induced by vertical mixing is not primarily controlled by the local wind, but rather by remotely forced coastal-trapped waves.

1. Introduction

The Congolese upwelling system (CoUS), located along the western African coast between 6°S and 4°S, just north of the mouth of the Congo River, is one of the most productive systems in the Gulf of Guinea (GG), and is likely to have a strong influence on regional fisheries (Voituriez & Herbland, 1982). The lowest sea surface temperature (SST) in the CoUS occurs during the austral winter (June–July–August) when the winds favorable for Ekman upwelling are weak (Berrit, 1976), as in the Angolan upwelling system (Awo et al., 2022; Ostrowski et al., 2009), suggesting that it is not associated with wind-driven Ekman transport, unlike the Benguela upwelling system further south (Bordbar et al., 2021; Carr & Kearns, 2003; Gutknecht et al., 2013). The Equatorial Undercurrent (EUC), which extends into the Gabon-Congo Coastal Undercurrent (GCUC) flowing southeastward, brings the source waters for the CoUS (Wacongne & Piton, 1992). The instability of the flow resulting from the vertical shear of the equatorial current systems between the EUC and the GCUC in the subsurface and the South Equatorial Current (SEC) at the surface could induce vertical mixing (Piton, 1988) and thus affect the SST. In the

CoUS, seasonal changes in SST can also be influenced by eastward-propagating equatorial Kelvin waves (EKW), which trigger poleward-propagating coastal-trapped waves (CTW) upon reaching the African coast (Picaut, 1983; Piton, 1988). Downwelling and upwelling CTWs cause the thermocline to deepen or shallow, respectively. These waves are often linked to SST changes, with downwelling waves being associated with surface warming and upwelling waves with surface cooling. North of the CoUS, between 3°S and 0°N, Herbert and Bourlès (2018) recently showed that the 2005 and 2006 surface cooling episodes were influenced by upwelling EKWs. Further south of the Congo River mouth, remotely and locally forced CTWs influence the ocean variability (at intra-seasonal, seasonal, and interannual timescales) of the Angola and Benguela upwelling systems (Bachelery et al., 2016; Illig et al., 2020; Körner et al., 2024; Ostrowski et al., 2009). Analysis of altimetry and tide gauge data, as well as model outputs, also reveals the semiannual cycle of sea level anomalies (SLA) characterized by the positive and negative SLA associated with CTW propagations along the African coast in the GG (Dieng et al., 2021).

Furthermore, the CoUS is also under the influence of the Congo River plume, a large tongue of low-salinity water, with high levels of sediments, organic matter, and nutrients. Indeed, the plume, driven by the topography, the Coriolis effect, and prevailing winds, generally extends northwestward, partially covering the Congolese continental shelf, and is potentially associated with mesoscale activity (Denamiel et al., 2013; Vic et al., 2014). Because of the thin mixed layer depth (MLD) due to the strong salinity stratification near the surface, the low-salinity plume can attenuate the vertical turbulent diffusivity, which increases and decreases with shear and stratification, respectively. This leads to a reduction in vertical mixing (Aroucha et al., 2024; Topé et al., 2023; Vallaeys et al., 2021; White & Toumi, 2014). From their observational analysis, Matera et al. (2012) associated positive interannual SST anomalies with years of high Congo River discharge and high precipitation in the GG. In contrast to Matera et al. (2012), White and Toumi (2014) did not find a significant effect of the Congo River on SST from their modeling experiments (with and without Congo River); this is consistent with the previous analysis by Hopkins et al. (2013) based on satellite observations. Their modeling results show that the impact of the Congo River on SST is limited to small regions under the influence of the River plume, and depends on the environmental conditions. The impact of high stratification due to the River plume has been highlighted to explain the 2016 interannual warm event off the coast of Angola (Lübbecke et al., 2019). The coastal southward extension of the minimum sea surface salinity (SSS) plume due to the Congo River and advected by the Angola Current, which is also controlled by CTWs, is influenced by interannual variability (Martins & Stammer, 2022). As previously mentioned, the high stratification due to Congo River can reduce vertical mixing, leading to a weakening of the coastal upwelling intensity. On the contrary, the density front around the Congo estuary could locally generate upwelling through the secondary ageostrophic circulation, in response to the increase in turbulence associated with the shear instability perturbing the initial geostrophic flow (Pham & Sarkar, 2018). The Congo plume could also induce coastal geostrophic divergence at its northern boundary, with possible enhancement of upwelling, in contrast to the opposite effect of the Niger River to its north on the opposite side of the equator (Alory et al., 2021). The seasonal SST minimum coincides with a maximum in chlorophyll-*a* (CHL-*a*) concentrations north of the Congo, as in other coastal regions of the GG (Brandt et al., 2023). Thus, understanding the seasonal variability of SST will also provide some insight into processes involved in nutrient flux and thus productivity in the CoUS.

In contrast to the Angola and Benguela systems, which have received more attention, the dynamics of the mixed layer temperature (MLT) in the CoUS is still debated. Several studies have focused on the influence of the Congo River at the scale of the tropical Atlantic basin. For example, Da-Allada et al. (2014) and Camara et al. (2015) used an ocean model to analyze seasonal changes in mixed layer salinity over large regions of the tropical Atlantic. In the southern GG, including the area of the Congo River plume, their results reveal that diffusion and vertical advection act against the action of horizontal advection and freshwater fluxes (mainly dominated by the Congo River) that freshen the mixed layer. These results are also in agreement with those of Houndegnonto et al. (2021) based on SMOS (Soil Moisture and Ocean Salinity) satellite observations. Also, the studies carried out to understand the seasonal cycle of the MLT have been limited to the larger regions around the Congo River. Using PIRATA (Prediction and Research Moored Array in the Tropical Atlantic, Bourlès et al., 2019) mooring data, Foltz et al. (2003) showed that the seasonal cycle of the MLT is controlled by the net surface heat flux, mainly the incoming shortwave radiation and the latent heat flux along 10°W at 10°S and 6°S. Peter et al. (2006) also found in numerical simulations that the mixed layer heat budget is governed by the net surface heat flux in the southern GG, and

especially at 3°E, between 8°S and 4°S. The dominant role of the net surface heat flux is also confirmed by Wade et al. (2011) in their box extending from 3°E to the African coast, between 10°S and 4°S. In addition, Ngakala et al. (2023) also emphasized this dominant role of net surface heat flux along the African coast, particularly in the Senegal, Angola, and Benguela regions, from simulated mixed layer heat budgets. In addition, Scannell and McPhaden (2018) used data from a PIRATA mooring located off the Congo River at (8°E; 6°S) to understand the seasonal variations of MLT. Their results show that the seasonal variations in net surface heat flux are strongly controlled by the incoming shortwave radiation and the latent heat flux, whose variations are influenced by the meridional displacement of the Intertropical Convergence Zone (ITCZ) and the low-level marine stratocumulus formation. In the boreal spring, they associate the warming of the mixed layer with the action of the incoming shortwave radiation, which is enhanced by the shallow MLD due to heavy precipitation and the freshwater input from the Congo River. During the austral winter, they attribute the cooling of the MLD to turbulent vertical entrainment (although not explicitly resolved) favored by upwelling conditions. Their study suggests the importance of taking into account precipitation to understand the mixed layer heat budget in the southeast of the Atlantic Ocean because of its effect on the MLD. In addition, results from numerical experiments based on ocean model simulations (with and without the Congo River) by White and Toumi (2014) suggest that the Congo River induces a slight cooling of the plume throughout the year by shallowing of the MLD, which reduces shortwave absorption in the mixed layer.

Further south, Körner et al. (2023) conducted a mixed layer heat budget analysis using available observations to understand the processes responsible for the cross-shore SST gradient observed in the Angolan upwelling system. Their results showed that cooling by turbulent mixing at the base of the mixed layer is stronger at the coast in the shallow regions of the shelf than offshore. However, the net surface heat flux attenuates the spatial differences in SST by inducing a stronger warming at the coast.

Here, for the first time, we use a high-resolution regional ocean model to identify the main atmospheric and oceanic processes controlling the seasonal evolution of the MLT in the CoUS. We focus our study along the Congolese coast between 6°S and 4°S, in the 1°-wide coastal band to capture the influence of CTWs (Bachelery et al., 2016; Illig et al., 2004). In the following, we describe the observations, the model, and the methodology used in Section 2. We then evaluate the model skills in reproducing the observations and analyze the MLT seasonal cycle and various processes involved in Section 3. Finally, Sections 4 and 5 are devoted to the discussion and conclusions/outlook, respectively.

2. Model, Data, and Methods

2.1. Model

We use a regional configuration of the NEMO ocean model (Nucleus for European Modeling of the Ocean, Madec et al., 2017) to understand the processes controlling the seasonal variability in the Congolese upwelling system. The regional simulation covers the GG from 11°S to 6°N, and from 10°W to the West African coast. The model solves the discretized primitive equations on a horizontal Arakawa C-grid following the generic length scale (GLS) turbulent closure scheme, with a horizontal resolution of 1/36° (~3 km). The vertical grid, in z coordinates, has 50 levels with 18 levels in upper 50 m. We use a k - ϵ -type turbulent closure within the GLS turbulence closure scheme to parameterize the vertical diffusion coefficient. The GLS scheme is considered as a general method, including several classical turbulence models, the k - kl , k - ϵ , and k - ω models (Umlauf & Burchard, 2003). The model is forced by daily MERCATOR GLORYS12V1 reanalysis outputs (Lellouche et al., 2021) with a horizontal resolution of 1/12° (~9 km) at its lateral open boundaries. Atmospheric fluxes used for surface forcing are from the Japanese Meteorological Agency JRA-55 reanalyses (Kobayashi et al., 2015), except for the daily surface winds which are from the ASCAT satellite product with a horizontal resolution of 1/4° or ~25 km (Bentamy & Fillon, 2012). The river runoff forcing for the model is provided by the daily outputs of the ISBA-CTRIP hydrological model (Decharme et al., 2019), except at the mouth of the Congo River (around 6°S), where the runoff is based on the daily flows measured by the Brazzaville station managed by the HYBAM network (HYdro-geochemistry of the AMazonian Basin) (Laraque et al., 2020). The simulation was run from 2005 to 2016 including two years of spin-up (2005–2006, initialized with GLORYS in 2005). The heat budget terms are computed online (5-min time step) at each depth level for the year 2016. The processes driving the seasonal changes of MLT along the Congolese coasts are inferred from the analysis

of the year 2016, due to the availability of heat budget terms. Analyzing the interannual SST variability over the 2007–2016 period shows that 2007 and 2016 years were relatively warm compared to other years (Figure S1 in Supporting Information S1) in our study region. This warm event in early 2016 was investigated in a previous study based on observations (in situ and satellite) in the southeastern tropical Atlantic off the coast of Angola and Namibia (Lübbecke et al., 2019). In the following, we will take into account this particularity of 2016 years. Note that this model configuration, with slightly different forcing, has already been used to study the impact of the Niger River warming effect in coastal upwelling systems north of the GG (Topé et al., 2023).

2.2. Data

Satellite and in situ observations are used to evaluate the ability of the model to realistically simulate the spatial and seasonal variations of some key surface and subsurface fields, such as SST, SSS, SLA, and temperature.

The Multiscale Ultrahigh Resolution (MUR) satellite product with $1/100^\circ$ spatial resolution (~ 1 km) and daily temporal resolution (Chin et al., 2017) is used to assess the realism of the model SST. This product is an optimal combination of SST data from infrared and microwave sensors. The observed SSS is derived from the Soil Moisture Active Passive (SMAP) satellite product with $1/4^\circ$ (~ 25 km) spatial and daily temporal resolution, which is obtained from a temporal extrapolation of 8-day products (Fore et al., 2016). Soil Moisture Active Passive sampling errors are globally about 0.01–0.02 psu at monthly timescales and are particularly high in regions of high SSS variability (Fournier et al., 2023). Although both of these satellite products have a daily resolution, we used the monthly MUR and SMAP products to validate the model SST over the period 2007–2016 (10 years) and SSS over the period 2016–2022 (i.e., 7 years, due to the availability of the SMAP product), respectively.

The CMEMS (Copernicus Marine Environment Monitoring Service) altimetry product, which combines data from several satellite missions with $1/4^\circ$ spatial and daily temporal resolution (Ducet et al., 2000; Le Traon et al., 1998), was used to evaluate the model SLA. For a better comparison between the model and the CMEMS product, we computed the SLA from the daily sea surface height over a common reference period (2007–2016). This SLA product is then used to assess the ability of the model to track the EKW eastward propagations and the subsequent CTW southward propagation along the African coast.

SSS from underway thermosalinographs (TSG) collected during 6 crossings of the Hawk Hunter commercial ship and 3 PIRATA cruises onboard French research ship in the GG during the austral winter (June–July–August) season between 2000 and 2021 are averaged along transects repeated at least 3 times (Alory et al., 2015; Bourlès et al., 2019; Gaillard et al., 2015).

In situ monthly climatological data from World Ocean Atlas 2018 (WOA18) with a horizontal resolution of $1/4^\circ$ (~ 25 km) and a vertical resolution of 5 m in the first 100 m (Garcia et al., 2019) are used for subsurface temperature validation.

In addition, we used daily in situ data from the PIRATA mooring (Rouault et al., 2009) located off the mouth of the Congo River at (8°E ; 6°S) over the 3-year period of 2014–2016 to consolidate the model validation in the surface and the subsurface. Following Scannell and McPhaden (2018), we first applied orthogonal linear least squares regression between 10 and 1 m and then 10 and 5 m to fill in the data gap for salinity at 1 and 5 m depth in 2016, respectively. And second, we linearly interpolated along the vertical with 1-m resolution from temperature and salinity profiles at depths of 1, 5, 10, 20, 40, 60, 80, 100, and 120 m. From this new time series, the associated subsurface daily density is computed and then the MLD and isothermal layer depth (ILD) are determined following Scannell and McPhaden (2018) using a density criterion (0.08 kg/m³) and a temperature criterion (0.3°C), respectively, relative to a reference depth of 1 m. The associated barrier layer thickness is defined as the difference between ILD and MLD.

2.3. Methods

The processes locally controlling the MLT along the Congolese coast within a 1° -wide band from the coast are examined from the mixed layer heat budget. This approach has already been used in several studies based either on observations (Scannell & McPhaden, 2018; Wade et al., 2011) or with our model (Jouanno et al., 2011; Peter et al., 2006). The evolution of the MLT is given by Equation 1:

$$\partial_t \langle T \rangle = \underbrace{\frac{Q^* + Q_s(1 - f_{z=-h})}{\rho_0 c_p h}}_A \underbrace{- \langle u \cdot \partial_x T \rangle - \langle v \cdot \partial_y T \rangle + \langle D_l(T) \rangle}_{B} \underbrace{- \langle w \cdot \partial_z T \rangle - \frac{(k_z \partial_z T)_{z=-h}}{h} - \frac{1}{h} \partial_t h (\langle T \rangle - T_{z=-h})}_{C} \quad (1)$$

where T is the potential temperature, (u, v, w) are the zonal, meridional, and vertical components of the velocity vector, respectively, $D_l(\cdot)$ is the lateral diffusion operator, and k_z is the vertical diffusion coefficient parametrized in the model following the GLS scheme (Umlauf & Burchard, 2003, 2005). ρ_0 , c_p , and h represent the surface reference density, the specific heat capacity, and the depth of the mixed layer, respectively. The fraction of the shortwave radiation that reaches the MLD is given by $f_{z=-h}$. The notation $\langle \cdot \rangle$ denotes the averaged quantities in the mixed layer of depth h . We calculated the MLD from daily outputs following a density criterion with 0.5 m (first level of the model) as reference level and 0.08 kg/m³ as threshold from daily vertical profile outputs as done in Scannell and McPhaden (2018). The heat budget terms are then integrated vertically over this MLD. In the discussion section, we will return to the choice and the sensitivity of the MLD criterion.

The left side of Equation 1 represents the MLT tendency term, and the right side represents all terms contributing to the mixed layer heat budget. A is the net surface forcing due to nonsolar surface fluxes (sum of longwave, latent, and sensible heat fluxes, Q^*) and the penetrating solar flux (Q_s). B includes the horizontal oceanic processes: the horizontal advection, composed of zonal and meridional components, and the lateral diffusion. C represents the sum of the vertical oceanic processes, that is, vertical advection, vertical diffusion at the base of the mixed layer, and entrainment. The latter represents temperature variations within the mixed layer due to changes in mixed layer thickness and is estimated as a residual to close the mixed layer budget (Jouanno et al., 2011).

In addition, we also investigated the link between surface and subsurface dynamics at the seasonal scale based on the three-dimensional (x -zonal, y -meridional, and z -vertical) online heat budget detailed in Equation 2. This showed how the MLT seasonal changes are related to the subsurface dynamics and also underlined the sensitivity of the mixed layer heat budget terms to the choice of the reference depth.

$$\partial_t T = \underbrace{\frac{Q^* + Q_s \times f(z)}{\rho_0 c_p}}_A \underbrace{- u \cdot \partial_x T - v \cdot \partial_y T + D_l(T)}_B \underbrace{- w \cdot \partial_z T - \partial_z (k_z \partial_z T) + Res(z)}_C \quad (2)$$

In Equation 2, the terms A , B , and C are similar to those described in Equation 1, but at each model vertical level, not averaged in the mixed layer. A depends on nonsolar fluxes only at the surface and decreases with depth. C includes the residual term, $(Res(z))$, representing the numerical diffusion associated with the temporal scheme, which is very small and will be disregarded.

Since seasonal changes in the MLT can also be influenced by remote forcing, such as the equatorially forced CTW, we analyze the signature of these waves along the equatorial band (8°W–12°E and 1°S–1°N) and along the Congolese coast (1°-wide coastal band between 6°S and 4°S) using SLA from both observations and the model. We also examine thermocline depth (TD) variations in the model. Previous studies have often used the 20°C isotherm as a proxy for the TD noted by Z_{20} (Herbert & Boulès, 2018; Lübbecke et al., 2019). Here, we used the basic definition of TD as the depth corresponding to the daily maximum vertical temperature gradient at each grid point, as in Illig and Bachèlery (2024). There are important differences between TD and Z_{20} in our coastal area illustrated in Figure S5 in Supporting Information S1.

3. Results

3.1. Evaluation of Model Skills

3.1.1. Surface Evaluation From Satellite Data

In austral winter (June–July–August), the model (Figure 1b) qualitatively reproduces the average SST conditions observed by the MUR satellite product (Figure 1a) in our study region. Indeed, the spatial analysis shows high SSTs offshore and low SSTs at the coast, which is typical of regions dominated by upwelling systems such as eastern boundary upwelling systems (EBUS; Chavez & Messié, 2009), in both observations and model.

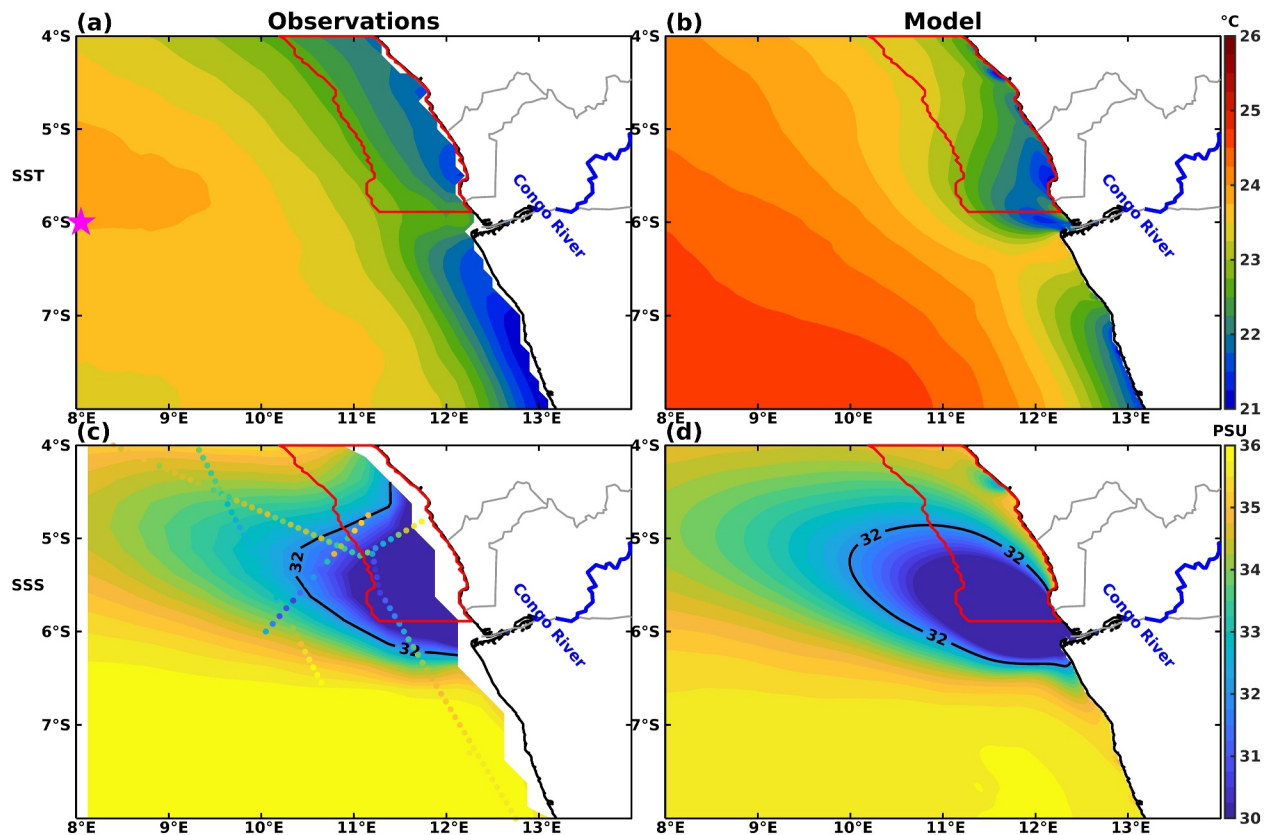


Figure 1. Mean austral winter (Jun–Jul–Aug) surface conditions (sea surface temperature (SST) (°C, top panels) and sea surface salinity (SSS) (PSU, bottom panels)) over the period 2007–2016 (except for SMAP SSS: 2016–2022) for observations (a) for Multiscale Ultrahigh Resolution SST and (c) for SMAP SSS and model SST (b) and SSS (d). Colored tracks in panel c are SSS from repeated TSG transects during the period 2000–2021. The 32 PSU isohaline delineates the extent of the Congo River plume. The red color represents the 6°S–4°S 1°-wide coastal box used in Figures 4, 8, and 9. The blue line is the Congo River and the magenta star in panel (a) are the PIRATA mooring positions at 8°E and 6°S.

This cooling could also be associated with upwelling CTWs as mentioned in the studies of Angola and Benguela upwelling systems (Bachelery et al., 2016). This cooling has a wider cross-shore extension and a more homogeneous alongshore extension in the observations than in the model. In the model, it is clearly stronger on each side of the Congo River mouth, which is slightly visible in the MUR product. Although the model and observations show similar large-scale structures, the model remains warmer offshore with a positive bias of about 1°C relative to the MUR product. These differences can be attributed to either the MUR product or the model. The global RMS difference (excluding the Arctic region) between MUR and other operational SST products is estimated between 0.39 and 0.52°C (Chin et al., 2017). Moreover, the MUR SST satellite product is based only on the nighttime (dusk to dawn locally) satellite SST. In the GG, the diurnal variation of near-surface temperatures due to daytime heating and nighttime cooling can reach a tenth degree (Wade et al., 2011), potentially influencing SST seasonal variability. Chin et al. (2017) suggest the inclusion of daytime MODIS to improve the future MUR SST analysis. In addition, the surface heat fluxes (Figure S8 in Supporting Information S1) used to force the model, or insufficient subsurface cooling, can lead to overestimating the SST. This may account for the larger difference between modeled and observed SST offshore than the coast. Comparing twin simulations, one with constant attenuation depths and the other with variable attenuation depths derived from ocean color data, and observations, Murtugudde et al. (2002) have shown that the model SST with variable attenuation depths compare better with observations in areas of high biological activity. Our model represents radiative processes in the ocean, accounting for the spectral variability of light and chlorophyll concentrations. The comparison between model and in situ PIRATA observations at the mooring location shows an underestimation of nonsolar fluxes (mainly latent heat flux), leading to an overestimation of the modeled air-sea heat flux relative to the observed air-sea heat flux.

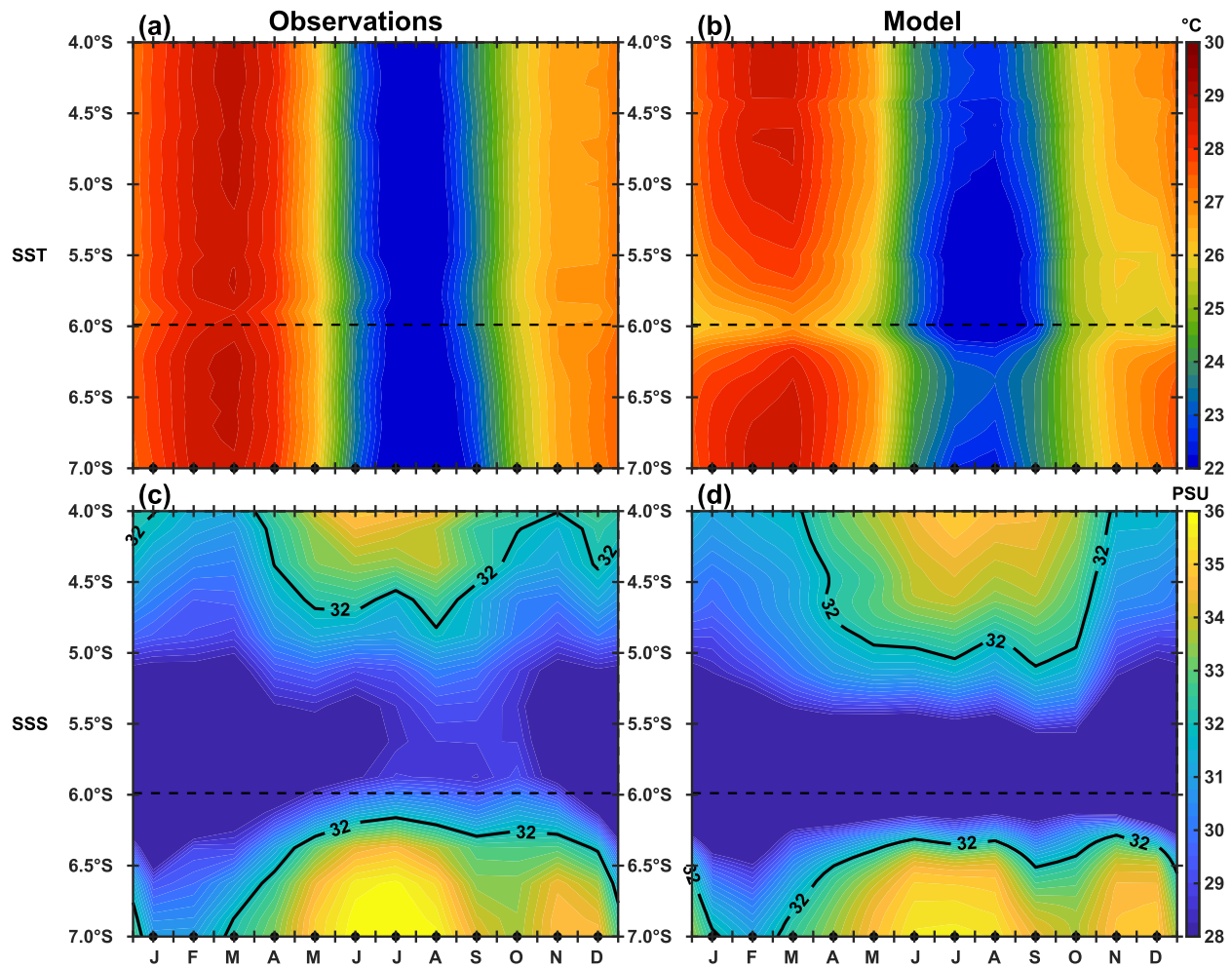


Figure 2. Monthly climatology of coastal (averaged within the 1°-wide coastal band) surface conditions (sea surface temperature (SST) (°C, top panels) and sea surface salinity (SSS) (PSU, bottom panels)) estimated over the period 2007–2016 (except for SMAP SSS: 2016–2022) for observations (a) for MUR SST, (c) for SMAP SSS and model SST (b), and SSS (d). The dashed line at 6°S highlights the location of the mouth of the Congo River. To facilitate comparison, the mask of the satellite data is applied to the model.

The model successfully reproduces the main features of the SSS (Figure 1d) on a large scale as observed by the SMAP satellite product (Figure 1c). We find saltier waters offshore and fresher waters at the coast due to the freshwater input from the Congo River. The model also captures well the northwestward extension of the Congo River plume (bounded by the 32 psu isohaline) associated with the southeast trade wind regime in agreement with previous studies in the region (Denamiel et al., 2013; Vic et al., 2014). Despite the model representing patterns similar to the observed mean SSS, it remains fresher than the SMAP mean, and this negative bias is amplified at the coast. These differences can be partially explained by the freshwater fluxes (dominated here by the Congo runoff) used as model forcing. Also, the SMAP climatological mean is heavily influenced by the Hybrid Coordinate Ocean Model (HYCOM) that provides the reference salinity field for the satellite product (Fore et al., 2016). Although the comparison could be biased by interannual variability due to their low sampling density, measurements along TSG transects suggest that the cross-shore SSS gradient is better reproduced by NEMO than HYCOM north of the river mouth.

Analysis of the coastal (1°-wide coastal band) monthly climatology of SST and SSS highlights the occurrence of cold and saltier waters during the austral winter in both satellite products (Figures 2a–2c) and model (Figures 2b–2d). In Figures 2a and 2b, low SSTs (<22°C) are observed between June and August, and high SSTs during the rest of the year. SSTs increase from September to a maximum (~28°C) around February–March, and decrease from April. North of 5°S (Figures 2c and 2d), the SSS structure appears to be influenced by the combined

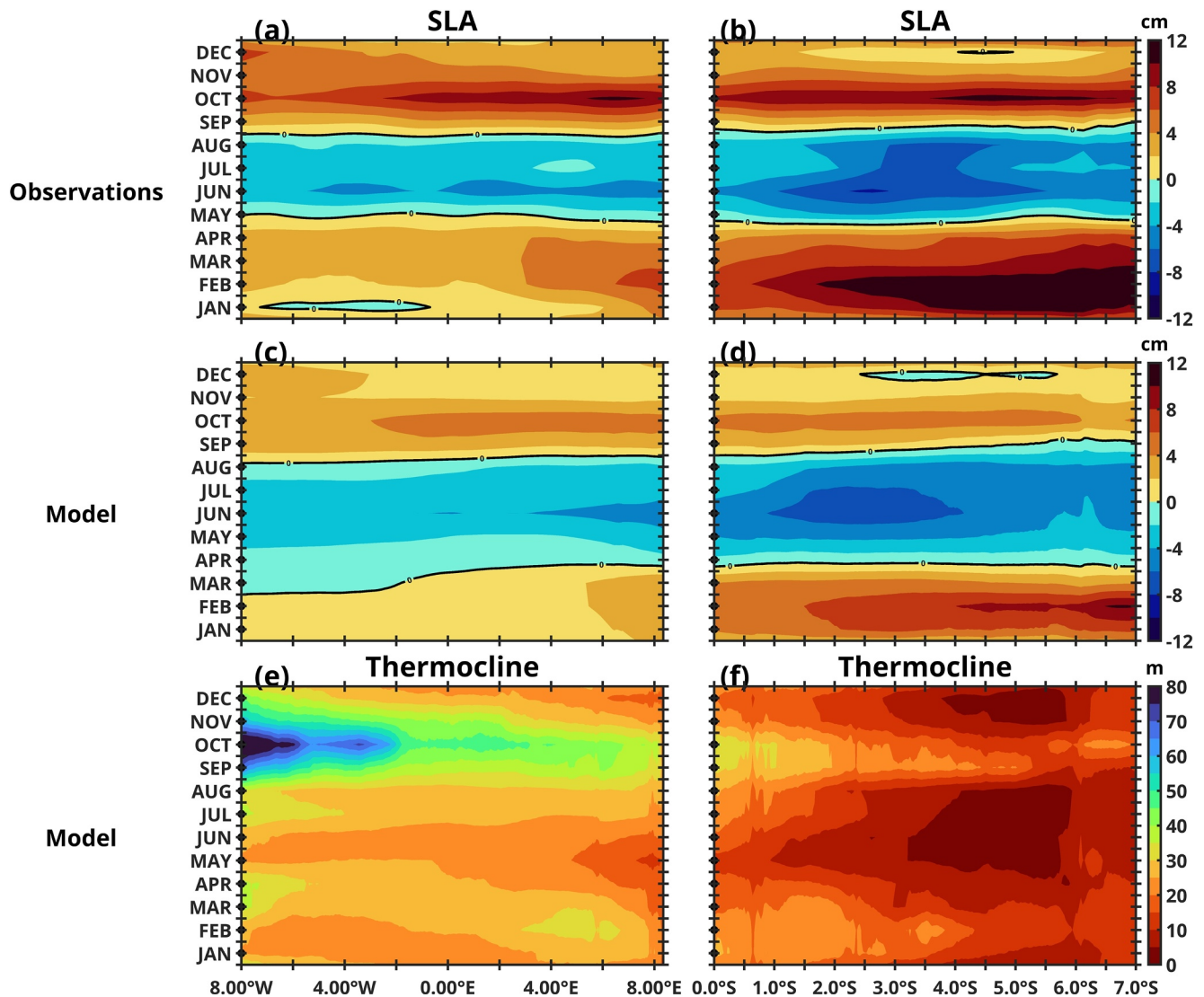


Figure 3. Eastern equatorial (averaged within 1°S–1°N, panels a, c, and e) and coastal (averaged within the 1°-wide coastal band, panels b, d, and f) monthly climatology of altimetry (CMEMS satellite product, panels a and b) and model (panels c and d) sea level anomaly (SLA, cm). Panels e and f show the model monthly climatology of eastern equatorial and coastal thermocline depth (TD, m), respectively.

coastal rainfall and Congo River regime. Saltier water is observed from May to early September, and fresher water appears during the rest of the year corresponding to the periods of maximum Congo River discharge (October–November–December) and coastal rainfall (February–March), which is consistent with previous studies in the Congo River area (Awo et al., 2022; Houndegnonto et al., 2021). South of the Congo River (less influenced by the plume than the north), fresher waters are observed from December to March and saltier waters during the rest of the year. The freshest waters due to the Congo River, presumably associated with strong salinity stratification, are found between 5°S and 6.5°S throughout the year. The occurrence of low-salinity waters due to the Congo River is strongly pronounced in the model compared to the SMAP product.

In order to investigate the connection to the equator, we focus on the seasonal analysis of the SLAs from both CMEMS observations (Figures 3a and 3b) and the model (Figures 3c and 3d), and of the simulated TD (Figures 3e and 3f) in the eastern part of the basin, along the equator (Figures 3a, 3c, and 3e) and along the southern African coast (Figures 3b–3f). Negative SLA in the CMEMS satellite product occurs in May–August along the equator (Figure 3a) and along the coast (Figure 3b), with an SLA minimum in June. With the exception of January between 7°W and 1°W and December between 5°S and 4°S, positive SLAs are observed the rest of the year,

with two maxima in February and October. Negative SLA anomalies appear earlier in the model, from March to August along the equator (Figure 3c) and then from April to August along the coast (Figure 3d). The model shows a positive SLA for the rest of the year except for December between 5.5°S and 2.5°S. The comparison between the model and the satellite products is limited by the lack of satellite data (CMEMS product) near the coast. In the model, the four seasonal crossings of CTWs, alternating between downwelling (SLA positive) and upwelling (SLA negative) seasons (Ostrowski et al., 2009), are visible along the coast. However, the second negative SLA minimum in 2016 is limited between 5.5°S and 2.5°S. It shows no obvious connection with the equatorial linear dynamics, although in general, this upwelling CTW in December is likely to originate from EKW forced by intensified trade winds during November–December (Okumura & Xie, 2006). The CTWs can also be locally forced by coastal meridional wind fluctuations in the southeastern tropical Atlantic (Bachèlery et al., 2016; Illig et al., 2020). At the equator (Figure 3e), the model shows shallow TDs between April and August, the main period of negative SLA anomalies. Deeper TDs are found during the rest of the year, except west of 4°E in January and east of 2°E in December. Along the coast (Figure 3f), the model shows that shallow TDs occur around April and August, and then in December, while deeper TDs occur the rest of the year. We note that the strong TD deepening and strong TD rising do not always coincide with the high positive and low negative SLA anomalies, respectively. In addition, the connection between EKW and CTW in December is more visible in TD than in SLA. The CTWs can be decomposed into different modes that affect the density fields in different ways. The faster low mode CTWs are visible in the SLA but do not affect variability in the near-surface layer, in particular, the density fields in the upper 300 m of the water column (Körner et al., 2024). In fact, for higher mode CTWs away from the shelf, the number of zero crossings in the vertical density structure increases (Illig et al., 2018). The steric height anomaly obtained from vertical integration of positive and negative density anomalies results in a cancellation effect, which consequently leads to a weak signature of these modes in SLA variability. In addition, the complex vertical structure of the high-order CTW modes, with smaller cross-shelf spatial scale (due to multiple zero crossings), results in pronounced temperature variations at certain depths. In contrast, low-order CTW modes have simpler vertical structure, with larger cross-shelf spatial scale (fewer zero crossings), and a more uniform influence on water column temperature or density. As a result, the high-order CTW modes better explain the near-surface pycnocline variability, while the low-order CTW modes account more for the SLA variability (Körner et al., 2024). Körner et al. (2024) analyzed the vertical structures of the different CTW modes in the Angolan upwelling system and found good agreement between the vertical structures of CTW modes 4 and 5 and the density anomalies on seasonal timescales. The analysis of the seasonal changes in the density field along the 5°S zonal section (Figures S3a–S3c in Supporting Information S1) and averaged over the study box (Figure S3d in Supporting Information S1) shows that the density varies with depth, season, and longitude (along 5°S). For example, the 26 kg/m³ isopycnal shoals from about 100 m in February–March (positive SLA and deep TD) to about 50 m in June–July–August (negative SLA and shallow TD) and becomes shallower toward the continental shelf (Figures S3a–S3c in Supporting Information S1). In Figure S3d in Supporting Information S1, the temperature also shows a variable vertical structure depending on the season. Although the spatial structures, phase, and group velocities of the respective CTW modes depend on several factors such as stratification, cross-shore topography, latitude, and mean flow (Brink, 1982, 2018; Illig et al., 2018), we assume that high-order mode CTWs control the seasonal variability of the vertical displacement of isopycnals (and isotherms) and thus influence thermocline as recently demonstrated in the Angola upwelling system (Körner et al., 2024). We will return to the role of the low and high mode CTWs in the Congolese upwelling system later.

3.1.2. Sub-Surface Evaluation From in Situ Data

A monthly climatology of near-surface temperature profiles averaged within our study area (1° wide coastal band from 6°S to 4°S, see Figure 1) also reveals the occurrence of low temperatures during austral winter (Figure 4). The model (Figure 4a) clearly reproduces the monthly evolution of the subsurface temperature observed in WOA climatology (Figure 4b), and in particular, the period of low temperature. However, the model is slightly colder than the WOA climatology for most of the year. These differences may be related to the poor density sampling of in situ data in the Congo River region or model bias.

Furthermore, the model also reproduces the seasonal evolution of the vertical profiles of temperature, salinity, and density observed by the PIRATA mooring at 8°E and 6°S (Figure 5). In June–August, the mixed layer cools (Figures 5a–5d) and becomes saltier (Figures 5b–5e), leading to denser waters (Figures 5c–5f) during this period. This also corresponds to the third annual rise of the thermocline, from July until October, which then deepens

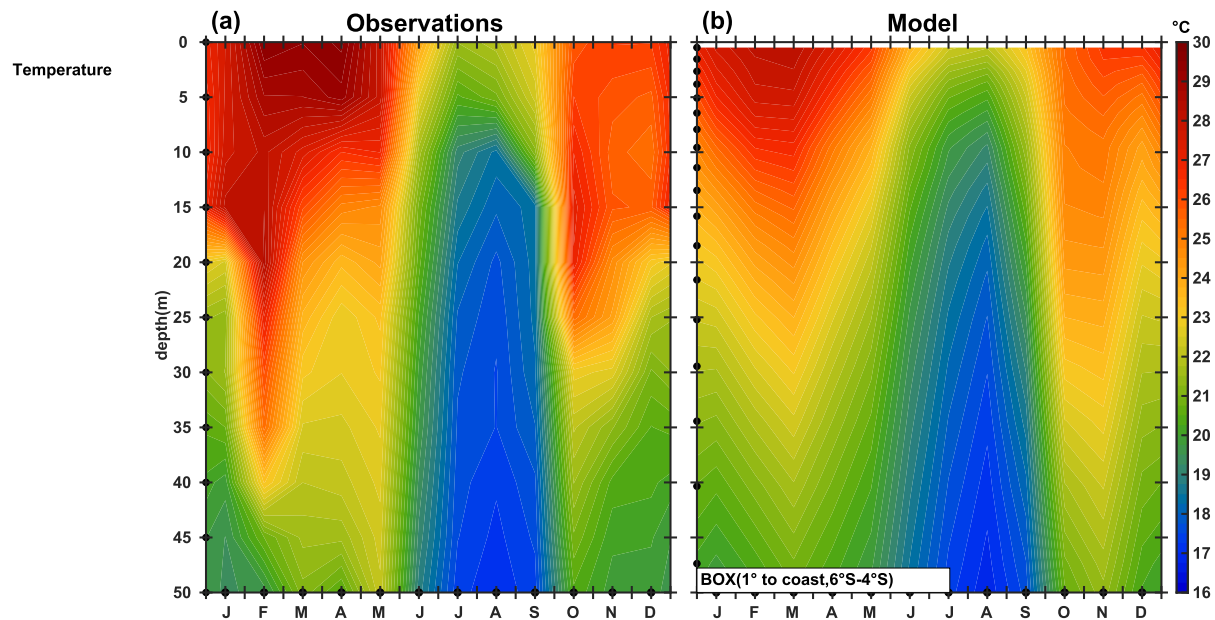


Figure 4. Temperature ($^{\circ}\text{C}$) monthly climatology averaged within the 6°S – 4°S 1° -wide coastal box (see Figure 1) following the vertical: (a) WOA and (b) the 2007–2016 model climatology.

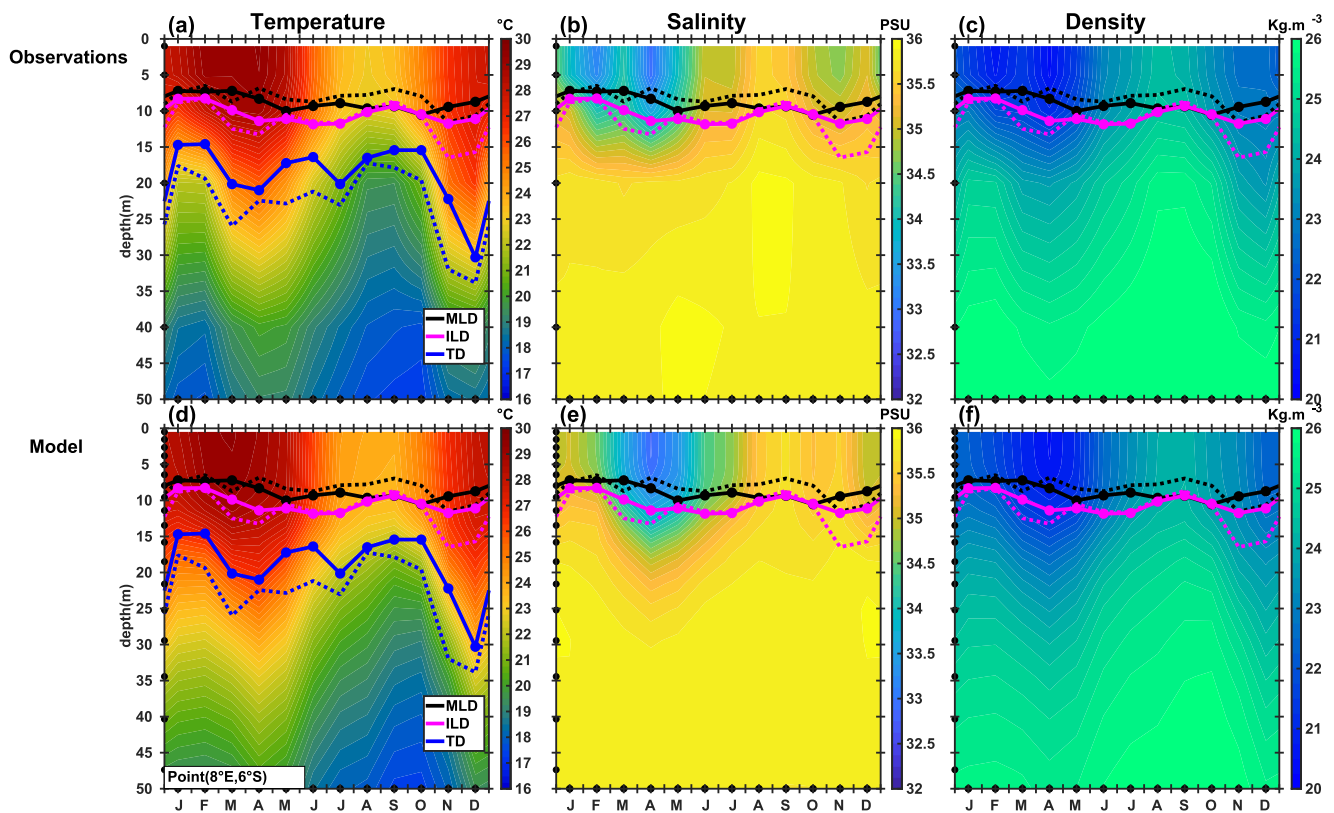


Figure 5. Monthly climatology of temperature (left panels, $^{\circ}\text{C}$), salinity (middle panels, PSU), and density (right panels, kg.m^{-3}) at 8°E ; 6°S as a function of depth (0–50 m) from PIRATA (top panels) and the model (bottom panels) for the period 2014–2016. Black, magenta, and blue lines represent the mixed layer depth (MLD), isothermal layer depth (ILD), and thermocline depth (TD), respectively, for the observations (dashed lines) and the model (solid lines). Due to the availability of the model outputs, the model MLD, ILD, and TD are computed offline from monthly profiles, rather than from daily profiles as for the PIRATA data.

steeply in both the PIRATA observations and the model. During the rest of the year, the mixed layer becomes warmer and fresher, and thus less dense. Also, the MLD, ILD, and TD in the model show a seasonal cycle in agreement with the PIRATA observations, although all 3 layers are deeper in PIRATA, especially outside of the upwelling season. Consequently, the modeled and observed BLTs are in phase during the seasonal cycle and reach their maximum in November–December, which is larger in the model. Although the model reproduces the salinity increase with depth, it remains saltier than PIRATA from December to February around 25–30 m depth. Note that, due to the availability of the model outputs, MLD, ILD, and TD are calculated offline from monthly profiles, rather than from daily profiles as in PIRATA. This can partly explain the difference between the model and the observations.

Despite the differences between the model and the observations, the model reproduces the observed surface and subsurface upwelling signature quite well. Thus, we can rely on our model to evaluate the processes responsible for the seasonal change of the MLT along the Congolese coast and to analyze how the surface dynamics are related to the subsurface dynamics in the Congolese upwelling system.

3.2. Interannual Variability in the Congolese Upwelling System: Insights From 2007 to 2016

To assess whether year 2016 is representative of a climatological seasonal cycle in the CoUS, we analyzed the interannual variations of SST, SSS, Congo River discharge, surface heat fluxes, MLD, and TD over the 2007–2016 period (Figures S1 and S2 in Supporting Information S1). The analysis reveals that 2007 and 2016 were warmer years, with the model showing slight temporal offsets in monthly SST anomalies compared to observations (Figure S1a in Supporting Information S1). Congo River discharge anomalies are generally out of phase with SSS anomalies and in phase with SST anomalies, particularly in 2007 and 2016. Freshwater inputs, driven by precipitation and river discharge, can indeed drive SSS and SST anomalies (Aroucha et al., 2024; Lübbecke et al., 2019). Nevertheless, the interannual correlation between SSS and SST anomalies is moderately weak (-0.57), underscoring the weak direct link between low-salinity plumes and high SST (Martins & Stammer, 2022). Furthermore, the interannual variability of Congo River discharge associated with the Indian Ocean Dipole in 2016/2017 is lesser pronounced than in 2019/2020 (Jarugula & McPhaden, 2023). The relatively average Congo River discharge (Figure S1e in Supporting Information S1) in 2016 coincided with average SSS (Figure S1c in Supporting Information S1) and significantly high SST (Figure S1a in Supporting Information S1), along with average heat fluxes (Figure S2a in Supporting Information S1), MLD, and TD (Figure S2c in Supporting Information S1). The analysis of the 2016 monthly anomalies (Figures S1b, S1d, S1f, and S2b–S2d in Supporting Information S1) shows that the 2016 austral winter (the period of interest for this study) is characterized by a relatively average river discharge, SSS, SST, surface heat fluxes, MLD, and TD. Overall, the CoUS in 2016 is therefore characterized by a relatively moderate river discharge, SSS, and SST, with otherwise rather average surface heat fluxes and subsurface conditions. At large scale, the tropical Atlantic equatorial mode did not show any significant activity during summer 2016 (Awo et al., 2018). Anyway, although the seasonal coastal upwelling systems in the eastern tropical Atlantic show interannual variability, they are characterized by a dominant seasonal variability (Brandt et al., 2023). Although some 2016 monthly anomalies exceed the average, we therefore expect the physical processes driving upwelling in 2016 to be fairly representative of the mean seasonal processes.

3.3. Mixed Layer Heat Budget Analysis

3.3.1. Processes Driving the Mixed Layer Temperature Seasonal Changes

In this section, we analyze the processes involved in the seasonal variation of the MLT (Figures 6 and 7) with a focus on the ocean continental margin along the Congolese coast. We use the model heat budget averaged within the mixed layer (see Section 2.3) to quantify the dominant processes responsible for the observed cooling in the CoUS. Note that lateral diffusion and entrainment contributions are found to be very weak compared to other process contributions (not shown).

As expected, the climatology of the coastal MLT (Figure 6a) is very similar to the SST cycle (Figures 2a–2c) along the coast. North of 6°S, we observe cold waters below 23.5°C between June and September, and warm waters the rest of the year. The MLT tendency (Figure 6b) shows mainly a cooling (negative values) between March and July and a warming (positive values) the rest of the year. However, we note a warming between 7°S and 6°S and then close to 5.5°S in April, another warming around 4.75°S–4°S in May, and a cooling around

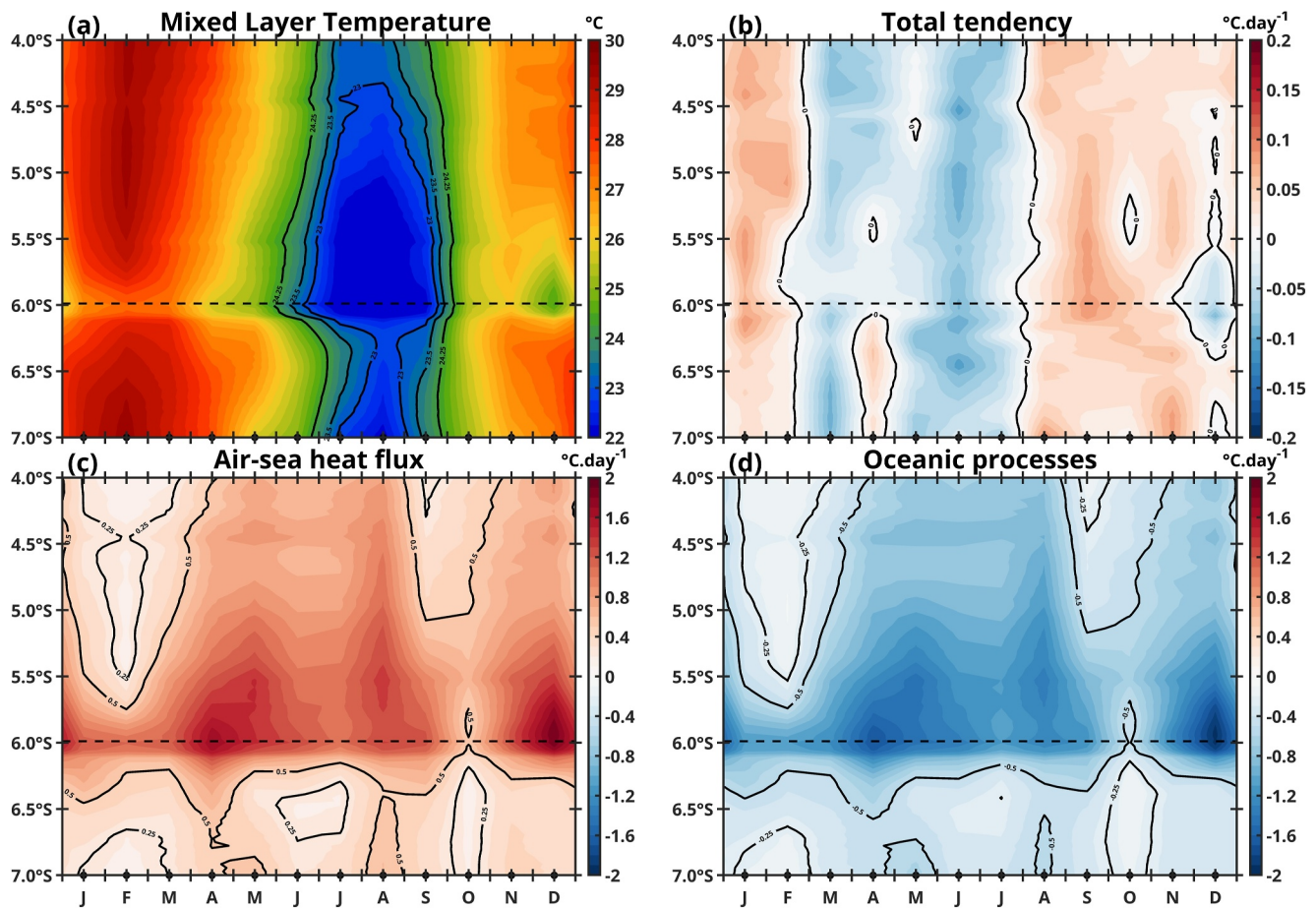


Figure 6. Model seasonal coastal mixed layer heat budget for the year 2016: (a) Mixed layer temperature (MLT, in $^{\circ}\text{C}$), (b) MLT tendency (in $^{\circ}\text{C}\cdot\text{day}^{-1}$), (c) net surface forcing term (A in Equation 1, in $^{\circ}\text{C}\cdot\text{day}^{-1}$), and (d) contribution of oceanic processes ($B + C$ in Equation 1, in $^{\circ}\text{C}\cdot\text{day}^{-1}$). All terms are longitudinally averaged within the 1° -wide coastal band from 7°S to 4°S .

6.15°S – 5.5°S in December. These seasonal changes in the tendency term reflect the balance of processes that drive the variations in the MLT. Air-sea heat fluxes (Figure 6c) warm the mixed layer throughout the year, and this means that the incoming shortwave radiations are dominant compared to nonsolar fluxes (latent heat, longwave, and sensible heat), which have a cooling effect. At the coast, the surface forcing (term A in Equation 2) variations are also controlled by the MLD associated with the strong salinity stratification of the Congo River discharge. A shallow MLD can warm faster and more intensely in response to incoming shortwave radiation, which probably explains the maximum in the river plume area just north of 6°S . As a result, the seasonal cooling is clearly due to oceanic processes (Figure 6d), which cool the MLD throughout the year and exceed the warming of the air-sea heat fluxes in March–July. The contribution of the horizontal processes (term B in Equation 2, Figure 7a) remains weaker than that of the vertical processes (term C in Equation 2, Figure 7d). North of 6°S , zonal advection (Figure 7b) cools throughout the seasonal cycle, and its effect is reduced or slightly enhanced by meridional advection (Figure 6c), which either warms or cools depending on the latitude during the season. However, zonal and meridional advectons intensively warm the mixed layer around 6°S . A comparison with a model simulation without runoff has revealed that at this latitude, the Congo River plume contributes to mixed layer warming through the advection of warmer freshwater (not shown). Vertical advection (Figure 7e) mostly cools the mixed layer, but its contribution is very weaker than the vertical diffusion contribution (Figure 7f). The latter mainly controls the seasonal cycle of vertical processes, so it is vertical diffusion that is responsible for the coastal cooling of the MLT between March and July. Along the 6°S zonal section, the mixed layer budget shows that the intensity of both air-sea heat fluxes and oceanic processes decreases away from the coast (Figures S6 and S7 in Supporting Information S1), as in the Angola upwelling system (Körner et al., 2023).

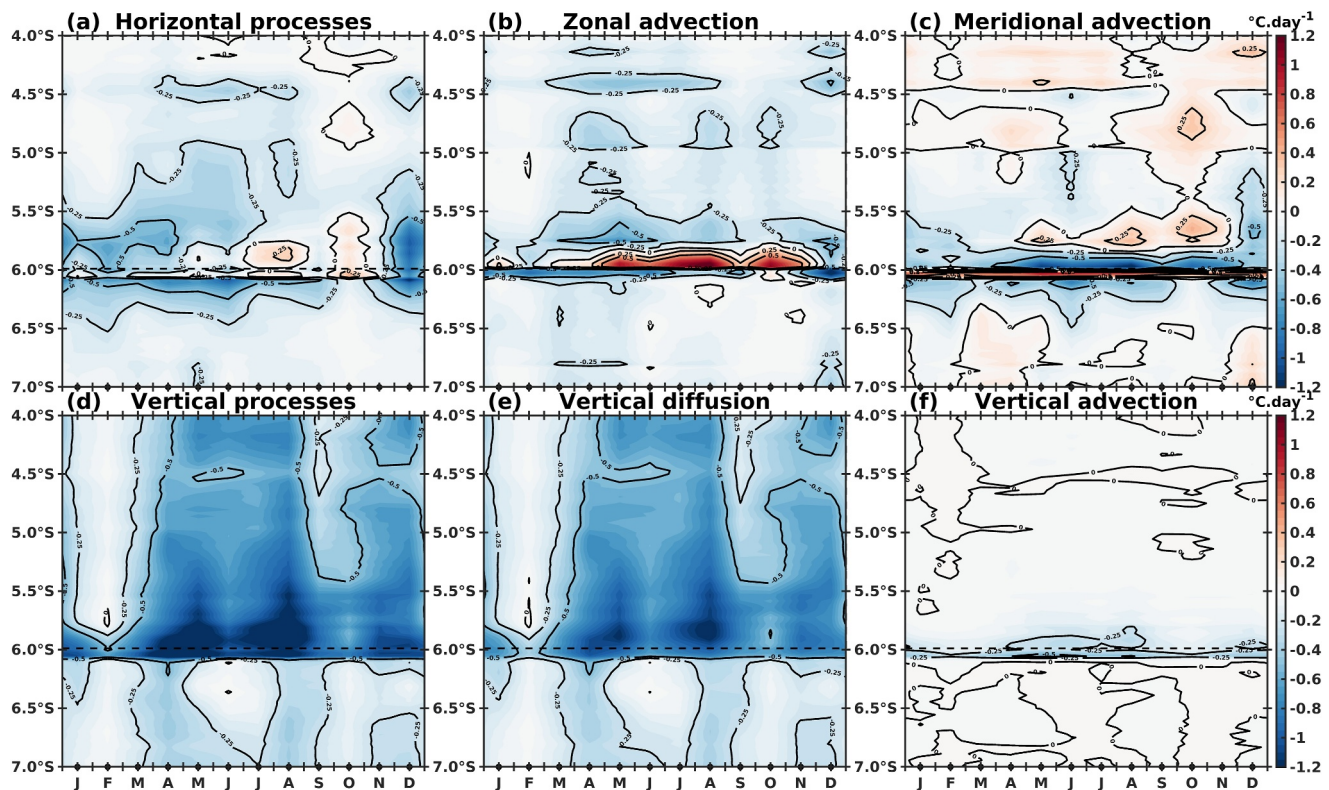


Figure 7. Model seasonal coastal mixed layer heat budget ($^{\circ}\text{C}\cdot\text{day}^{-1}$) for the year 2016: (a) Contribution of horizontal oceanic processes (B in Equation 1), (b) zonal advection, (c) meridional advection, (d) sum of all vertical oceanic processes (C in Equation 1), (e) vertical diffusion, and (f) vertical advection. All terms are longitudinally averaged within the 1° -wide coastal band from 7°S to 4°S .

In conclusion, this analysis clearly shows a competition between two main terms: air-sea heat fluxes and vertical diffusion at the base of the mixed layer, which controls the seasonal variations of the MLT along the Congolese coast. The strong cooling by vertical mixing in combination with the weak cooling by advection exceeds the strong warming by incoming shortwave radiation during March–July.

3.3.2. Seasonal Variations of Subsurface Processes

We have shown that the mixed layer cooling during March–July can mainly be explained by strong vertical diffusion combined with a weaker effect of advection. We now explore the possible link between the mixed layer cooling and the subsurface dynamics in the Congolese upwelling system (Figure 8). In particular, we emphasize the sensitivity of the MLD criterion to how cooling at the base of the mixed layer relates to the underlying subsurface processes.

Figure 8a shows similar characteristics to Figures 4a and 4b with a dominant semiannual seasonal cycle, although the year 2016 is slightly warmer than the 2007–2016 climatology. In Figure 8b, the temperature tendency term over the vertical shows a cooling over a long period between March and July from the surface to at least 50 m depth. We remark a further cooling in November–December below 5–10 m. On the other hand, we note a warming between 0 and 50 m in January–February, and a stronger warming around September, which persists down to depths greater than 50 m. This stronger warming results from warming by meridional advection combined with the weak warming by zonal advection (Figure S4 in Supporting Information S1). Between 10 and 50 m, zonal advection (Figure S4b in Supporting Information S1) warms in March–April and in October–November. Below the mixed layer, the cooling effect due to zonal advection in the 30-m range is offset by the warming due to meridional advection (Figure S4c in Supporting Information S1). Here, we focus on the March–July cooling between 0 and 50 m, whose intensity decreases with depth but is still present until at least 100 m depth (Figure S5 in Supporting Information S1). Now, we see that different vertical oceanic processes drive cooling in the surface and in the subsurface. Vertical diffusion (Figure 8c) strongly cools the mixed layer, which

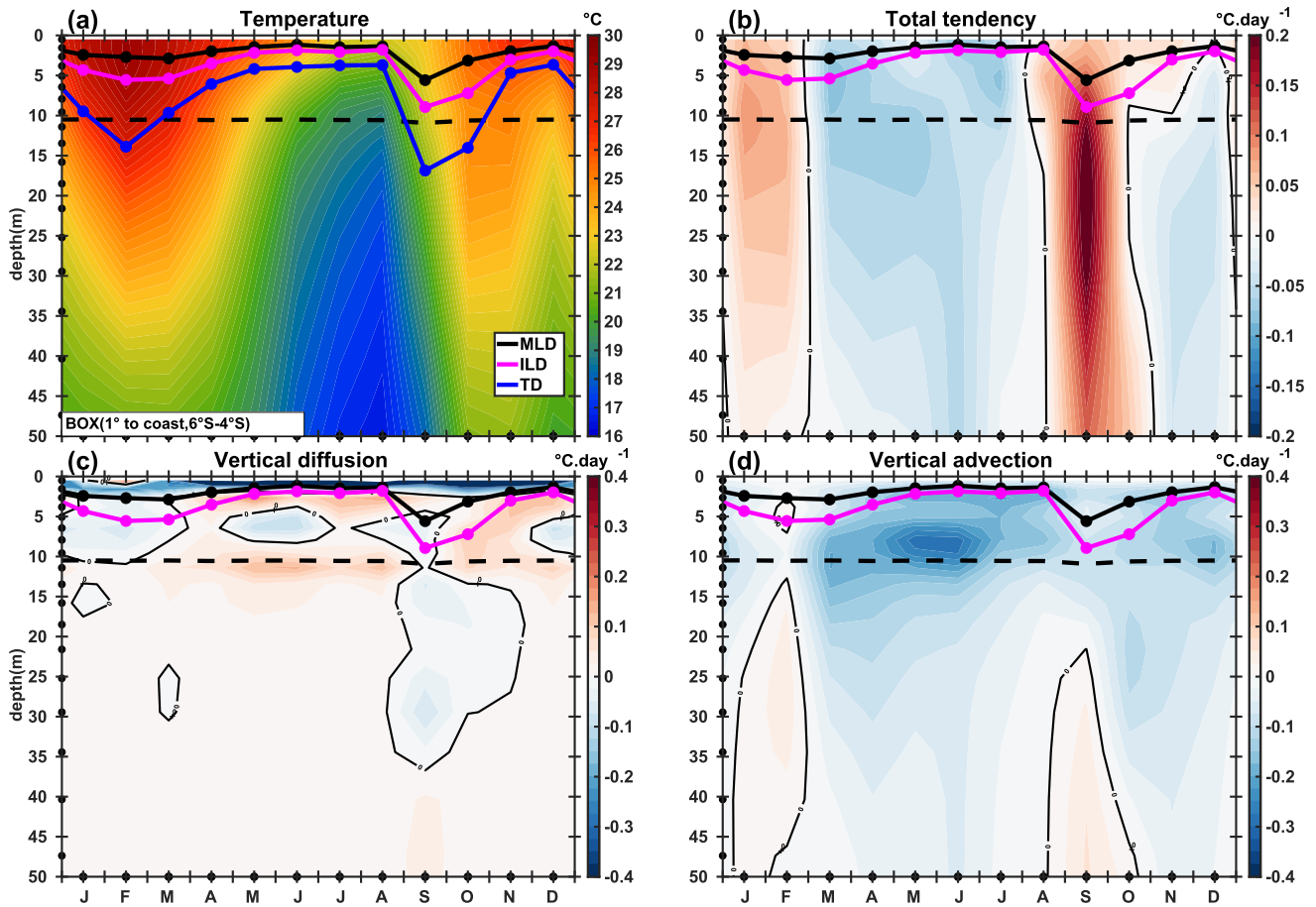


Figure 8. Time evolution of model coastal heat budget for the year 2016 as a function of depth (0–50 m), averaged within the 6°S–4°S 1°-wide coastal box (see Figure 1): (a) Temperature (°C), (b) temperature tendency (°C.day⁻¹), (c) vertical diffusion (°C.day⁻¹), and (d) vertical advection (°C.day⁻¹). Black, magenta, and blue lines denote the mixed layer depth (MLD), isothermal layer depth, and thermocline depth, respectively. The dashed black line represents the MLD calculated online according to the density criterion with a threshold of 0.01 kg/m⁻³ and a reference depth of 10 m.

largely offsets the strong warming effect of the surface heat fluxes. However, below the mixed layer, vertical diffusion generally warms the subsurface, although it cools it at certain depths and seasons. Vertical advection (Figure 8d) warms the water between 15–50 m and 30–50 m, in January–February and September, respectively. Otherwise, vertical advection predominantly cools the water column, and this cooling is most pronounced below the mixed layer in the 5–15 m interval approximately from March to July, and around December. From this subsurface analysis, it can be concluded that cooling by vertical mixing is mostly confined to the mixed layer throughout the seasonal cycle.

Although cooling by vertical advection is weak at the base of the mixed layer, the subsurface cooling by vertical advection is required to explain the enhanced cooling by vertical mixing at the base of the mixed layer. Note that the effect of vertical mixing on the MLT (within term C of Equation 1) depends on the parameterized vertical diffusion coefficient noted k_z , the vertical temperature gradient at the base of the mixed layer, and the MLD. k_z , representing the turbulence, depends on time evolution of turbulent kinetic energy and mixing length by the GLS scheme.

To better understand the seasonal dynamics of vertical diffusion in the MLD, we analyzed the seasonal cycle of stratification, vertical shear, wind stress, and k_z . Stratification is represented by the Brunt-Väisälä frequency (N^2), defined as $N^2 = -\frac{g}{\rho} \frac{\partial \rho}{\partial z}$, where g the gravity and ρ the density. Near-surface stratification depends on surface buoyancy fluxes. N^2 shows seasonal maxima in May–July and November–December (Figure 9a). The second maximum is primarily controlled by salinity stratification due to strong freshwater input from precipitation and the Congo River. The first maximum is rather explained by incoming shortwave radiation as freshwater flux is

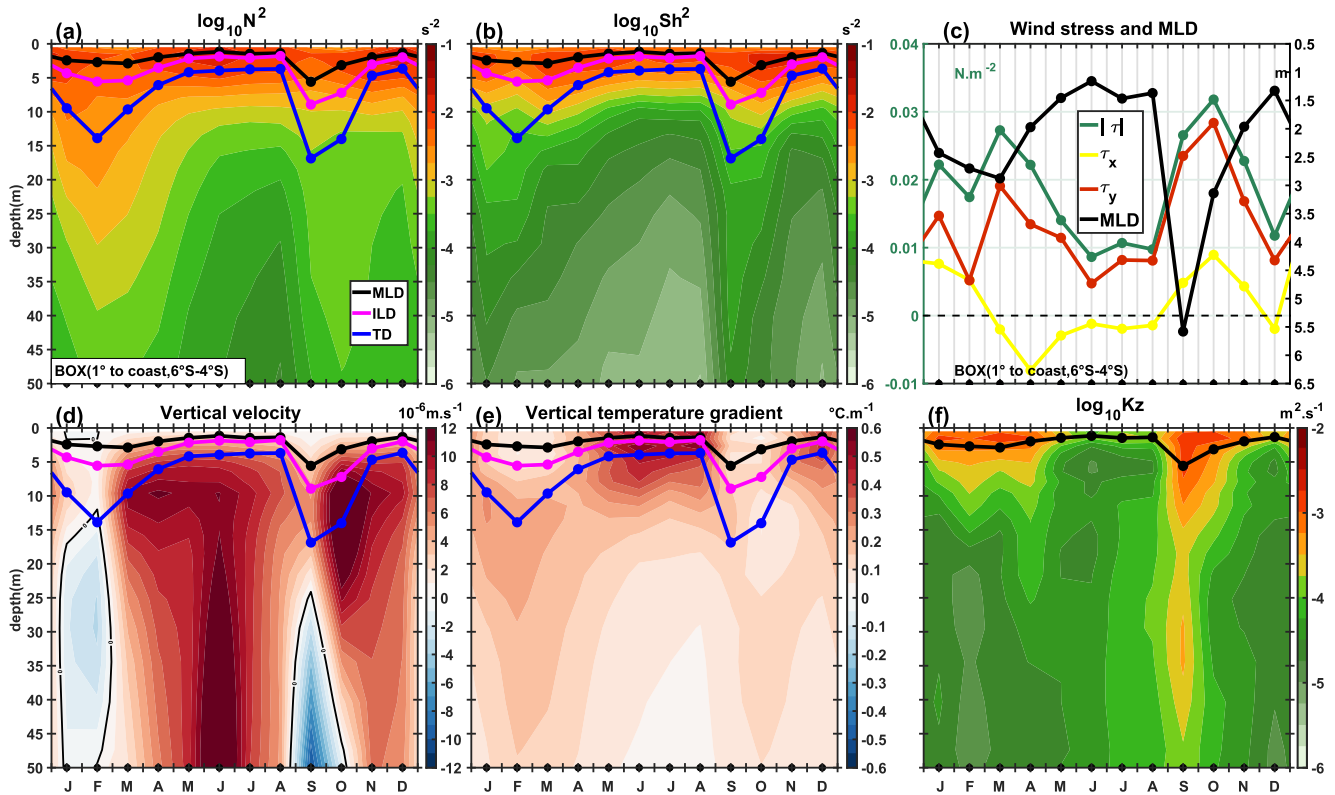


Figure 9. Model monthly climatology of vertical profiles (0–50 m), wind stress, and mixed layer depth (MLD) for the year 2016 averaged within the 6°S–4°S 1°-wide coastal box (see Figure 1): (a) Brunt-Väisälä frequency (N^2 , in s^{-2}), (b) total square vertical shear (Sh^2 , in s^{-2}), (c) wind stress ($N \cdot m^{-2}$) magnitude (green) with zonal (yellow) and meridional (red) contributions, and MLD (black, in m), (d) vertical velocity (in $10^{-6} m \cdot s^{-1}$), (e) vertical temperature gradient (in $^{\circ}C \cdot m^{-1}$), and (f) vertical diffusion coefficient (k_z , in $m^2 \cdot s^{-1}$). In panels a, b, d, and e, the black, magenta, and blue lines denote the MLD, isothermal layer depth, and thermocline depth, respectively.

dominated by evaporation during this period (not shown). Vertical shear (Sh^2 , Figure 9b), defined as $Sh^2 = \left[\left(\frac{\partial u}{\partial z} \right)^2 + \left(\frac{\partial v}{\partial z} \right)^2 \right]$, favors mixing that tends to break stratification. It peaks in March–April and October–November, roughly corresponding to the seasonal peaks in local wind stress that are expected to increase surface currents (Figure 9c). However, in September, despite strong wind stress, Sh^2 is smaller, which may be due to the influence of CTWs on shear stress. Note also that the predominantly northward wind stress is minimum during the June–July–August low SST season, in contrast with Ekman-driven upwelling systems (Berit, 1976). Turbulent mixing is enhanced by shear stress and damped by stratification; therefore, the seasonal maxima of k_z correspond to periods when Sh^2 overcomes N^2 (Figure 9f). k_z and MLD are closely linked, as illustrated by their simultaneous maximum in September, moderate values in January–April, and minimum in May–August.

Below the MLD, cooling is driven by vertical advection (Figure 8d) that is the product of vertical velocity (Figure 9d) and temperature gradient (Figure 9e). During May–June, when vertical advection is maximum around 5–10 m depth due to both strong velocity and temperature gradient, upwelling (Figure 9d) intensifies stratification by bringing colder water close to the surface. This also corresponds to a rise in the TD. This results in a maximum in vertical temperature gradients in May–August at the base of the mixed layer (Figure 9e), which, combined with a minimum in MLD and relatively weak but sufficient k_z (Figure 9f), leads to the seasonal maximum in cooling by vertical diffusion (Figure 7e).

The above results suggest the importance of remote forcing. Indeed, the analysis of the seasonal cycle of the modeled TD (Figures 3e and 3f) clearly shows the semiannual cycle of EKWs propagating eastward along the equator and then southward along the African coast as CTWs, with strong upwelling (shallower TD) during the austral winter surface cooling (Figures 6b and 8b), between two downwelling phases (deeper TD). The upwelling associated with the CTWs is concomitant with the upward vertical velocities from April to August (Figure 9d),

the rise of the thermocline and the strengthening of the vertical temperature gradient at the base of the mixed layer (Figure 9c), and the resulting mixed layer cooling by vertical mixing.

4. Discussion

We investigated the seasonal changes of the MLT in the CoUS, in a 6°S–4°S 1°-wide coastal box just north of the Congo estuary, and in particular, the austral winter cooling leading to SSTs as cold as ~22°C, through the mixed layer heat budget of a high-resolution oceanic model. The heat budget analysis reveals a competition between two main processes, as other tendency terms are weaker (Figures 6 and 7). These processes are the surface forcing dominated by incoming shortwave radiation (Figure 6a), which is counterbalanced by vertical mixing at the base of the mixed layer (Figure 7e). The latter, in combination with a weak contribution from advection, is mainly responsible for the seasonal cooling resulting in the low SSTs in austral winter.

Air-sea heat fluxes are dominated by incoming shortwave radiation and therefore tend to warm the mixed layer all year long in our region. This warming is stronger around the Congo River mouth probably due to the thin mixed layer associated with the strong salinity stratification in the river plume (Figures 9a and 9b). Previously, Scannell and McPhaden (2018), using in situ measurements at the PIRATA mooring about 500 km off the mouth of the Congo River, found that the latent heat flux drives the cooling of the mixed layer in austral winter. Herbert and Bourlès (2018), using an oceanic model, found the same result in a large coastal box (5°E–14°E; 7°S–0°N) including both the mooring and our own box in the southeast corner. These results differ from ours, but there is no contradiction. Indeed, recently, Körner et al. (2023) also made, from combined satellite and in situ data, a comparative mixed layer heat budget between an offshore and a coastal box located in the Angola region south of ours (15°S–8°S). They found that the incoming shortwave radiation warming is stronger while the latent heat flux cooling is weaker in the coastal box than the offshore box, respectively, due to a stronger cloud cover away from the coast, and weaker wind near the coast. ASCAT satellite winds that are used to force our model were specifically selected to include this wind drop-off at the coast, due to increased friction with land, that can notably affect coastal upwelling through Ekman pumping in the Benguela region (Fennel et al., 2012). These cross-shore variations result, in the Angola upwelling system, in net air-sea heat fluxes that can cool the ocean for a few months offshore but warm it all year long at the coast, especially when combined with the salinity stratification effect, like in our region. This is also in agreement with the study of Lübbecke et al. (2019) in the Angola region, which explains the warm event in early 2016 by the combined action of reduced latent heat flux due to weakened wind and the freshwater input due to local precipitation and river discharge (dominated by the Congo River). Note, however, that the net downward air-sea heat flux could be overestimated in the model, as suggested by the 1°C warm offshore SST bias in the model compared to satellite data (Figures 1a and 1b), although this bias is reduced at the coast (Figures 2a and 2b).

However, cooling by strong vertical mixing combined with weak mixed layer advection exceeds warming by air-sea fluxes between March and July, which then leads to mixed layer cooling along the CoUS (Figures 6 and 7). To understand the vertical mixing-induced cooling, we have examined the influence of local and remote forcing at seasonal scale. Comparison of seasonal variations of the vertical shear of horizontal currents, partly controlled by wind stress, and the mostly salinity-driven stratification shows that the former does not dominate over the latter during the cooling season (Figure 9). Indeed, wind stress peaks in March and October when vertical temperature diffusion is weak and, conversely, vertical temperature diffusion becomes strong from May to August when wind stress is weak (Figures 7e and 9a–9c) north of 6°S. The salinity-driven stratification due to strong freshwater inputs from precipitation and Congo River reduces the vertical mixing through the barrier layer (Lübbecke et al., 2019; Matera et al., 2012; White & Toumi, 2014). Recently, Aroucha et al. (2024) have proposed two explanations for the reduced vertical mixing in the 1995 Benguela Niño: a weakening of the vertical gradient temperature at the base of the mixed layer due to a thicker barrier layer, and a reduction in the vertical diffusion coefficient due to increased stratification. Here, the barrier layer is out of phase with the stratification. The barrier layer is thickest in February and September, and the barrier layer is almost absent during the seasonal cooling (Figure 8). We note a strong cooling by vertical mixing in the mixed layer throughout the year, with minima in January–February and September (Figure 7e). The barrier layer and vertical mixing appear to be under the control of the vertical temperature gradient that is driven by the thermocline motion (Figure 9). The seasonal maxima in vertical temperature diffusion, in May–August and November–December (Figure 7e), match those of the vertical temperature gradient at the base of the MLD, when the TD is shallower (Figure 9e). Since the low mode CTWs uniformly affect the temperature water column, the vertical advection during the austral winter is due to

equatorially forced upwelling high mode CTWs. This leads to a shallow thermocline, which induces a strong vertical temperature gradient in the upper 10 m. Combined with the wind-induced mixing, albeit weak, this results in the strong shallow cooling by vertical mixing. Consequently, the surface cooling and the seasonal SST minimum in the CoUS are caused by the strong cooling due to vertical mixing at the base of the mixed layer combined with the weak mixed layer advection cooling. This result provides a clear explanation for the upward movement of the isotherms from 200 m depth to the surface that is observed in the CoUS (Piton, 1988). The remote influence of EKW on SST seasonal changes have been already found further south in the Angola and Benguela upwelling systems (Bachelery et al., 2016; Illig et al., 2020; Ostrowski et al., 2009). Also north of the CoUS, between 3°S and 0°N, Herbert and Bourlès (2018) have shown that surface cooling events in 2005 and 2006 were influenced by subsurface oceanic conditions linked to the arrival of upwelling EKW. More recently, Körner et al. (2024) have explained the seasonal productivity of the Angolan upwelling system by the combination of the faster low mode CTW and the slower high mode CTW. Future studies could focus on identifying the different high modes involved, determining how they affect thermocline variability, and their connection to the low mode CTWs in the CoUS.

From our subsurface analysis, we have identified two main vertical oceanic processes that can cool the upper ocean: vertical diffusion (Figure 8c) and vertical advection (Figure 8d). Vertical diffusion has a strong cooling effect limited to the upper 3 m all year long, with a maximum from April to August, but often a weak warming effect below and particularly at 10 m depth. Vertical advection has mostly a cooling effect in the upper 50 m, particularly strong around 10 m from April to August, which is associated with the rise of the thermocline by upwelling CTWs discussed above (strong vertical temperature gradient and upward velocities in Figures 9d and 9e). The relative contribution of these two processes to the mixed layer heat budget is highly dependent on the definition of the MLD, and particularly, the chosen reference depth, which is still the subject of a debate in the GG. In this region, earlier mixed layer heat budget studies based on model or observation often used a density criterion relative to a reference depth of 10 m (Alory et al., 2021; Kanga et al., 2021; Lübbecke et al., 2019; Matera et al., 2012; White & Toumi, 2014), as globally recommended by de Boyer Montégut et al. (2004) to avoid diurnal variations when MLD is estimated from Argo profiles. However, in our highly stratified Congo River plume region, the MLD computed online in the model with this reference depth and a density criterion of 0.01 kg/m^{-3} is almost constant and very close to 10 m (Figure 8). Vertical advection would be considered the dominant cooling term for the mixed layer in this case. But the thermocline is often shallower than 10 m, which is inconsistent, and the vertical shear from the wind-driven current is concentrated in a thinner layer (Figure 9b). This strongly suggests that the MLD should be computed differently here. Therefore, we defined the MLD with a reference depth at the surface (actually 0.5 m that is the first depth level in the model), like other recent studies around the Congo plume region (Körner et al., 2023; Scannell & McPhaden, 2018), which puts the emphasis on the dominant role of vertical diffusion on the cooling in the mixed layer.

5. Conclusions and Outlook

A high-resolution regional ocean model is used to investigate the seasonal changes of MLT in the Congolese upwelling system, north of the Congo River. The model is comparable with available observations in terms of spatial and seasonal variations of oceanic variables and remotely forced CTW along the coast in a well manner. The mixed layer heat budget analysis allows to identify the main processes driving these seasonal variations.

The mixed layer heat budget analysis reveals a competition between warming by surface heat fluxes, dominated all year long by the incoming shortwave radiation, and cooling by the vertical mixing at the base of the mixed layer, because other tendency terms are weak throughout the year. The seasonal cooling is induced by vertical mixing combined with weak mixed layer advection, with the local wind dynamics assumed to play a secondary role. A subsurface analysis shows that vertical advection by remotely forced coastally trapped waves rise the thermocline from April to August, which strengthens the vertical temperature gradient at the mixed layer base and leads to the mixing-induced seasonal cooling in the Congolese upwelling system. These main driving processes, deduced from our model, are similar to those deduced from a recent observation-based study for the Angola upwelling system further south, on the other side of the Congo River mouth (Körner et al., 2023, 2024).

However, in the Angola upwelling system, Zeng et al. (2021) have suggested that internal tides can induce the strong mixing in shallow areas, cooling the mixed layer near the coast. By using microstructure measurements of shear to estimate turbulent heat fluxes, Körner et al. (2023) have indeed found that the cooling due to turbulent mixing at the base of the mixed layer is stronger at the coast in the shallow area than offshore. Our model

can reproduce the seasonal cooling without tides, but a sensitivity experiment including tidal forcing could be conducted to evaluate the contribution of internal tides in the CoUS. Recently, Alory et al. (2021) and Topé et al. (2023) used twin simulations with and without rivers to quantify the role of the Niger River discharge along the northern coast of the GG. Their results show that the river runoff induces warming by reducing the vertical mixing and the onshore meridional advection. There are contrasting results on the Congo River effect suggesting either SST warming (Materia et al., 2012) or cooling (White & Toumi, 2014), and we plan to evaluate this effect on the mixed layer heat budget in our model, with sensitivity experiments now available. We could also modify the equatorial wind forcing in our model to suppress EKW and quantify their effects along the Congolese coast. It would also be interesting to determine the role of different CTW modes in CoUS. Finally, a reference coupled physical-biogeochemical simulation based on our model configuration is in preparation, which would help to assess the respective biological contribution of upwelling and Congo River nutrient inputs in our region.

Acronyms:

CTW	Coastal-trapped waves
CoUS	Congolese upwelling system
EBUS	Eastern boundary upwelling system
EKW	Equatorial Kelvin waves
GG	Gulf of Guinea
ILD	Isothermal layer depth
MLD	Mixed layer depth
MLT	Mixed layer temperature
SSS	Sea surface salinity
SST	Sea surface temperature
TD	Thermocline depth

Data Availability Statement

All products used here are publicly available, and some require free registration. The MUR SST product created by the JPL MUR MEaSURES program as part of the GHRSSST (Group for High-Resolution Sea Surface Temperature) project is obtained from <https://podaac.jpl.nasa.gov/dataset/MUR-JPL-L4-GLOB-v4.1>. The SMAP SSS product created by JPL (Jet Propulsion Laboratory) is available at https://podaac.jpl.nasa.gov/dataset/SMAP_JPL_L2B_SSS_CAP_V5. The CMEMS (Copernicus Marine Environment Monitoring Service) SSH product produced by SSALTO/DUAC is available at <http://marine.copernicus.eu/>. The TSG SSS product managed by SNO-SSS/SEDOO is available at <http://sss.sedoo.fr/>. PIRATA surface and subsurface data are from <https://www.pmel.noaa.gov/tao/drupal/disdel/allsites/>. The WOA data are from NOAA/NCEI via <https://www.nodc.noaa.gov/OC5/woa18/>. Model outputs are available from the authors, especially GA, ID, GM, and JJ.

Acknowledgments

This work is part of Roy Dorgeless Ngakala's Ph.D. thesis funded by the German Academic Exchange Service (DAAD) under the In-Country/In-Region Scholarship Program for Sub-Saharan Africa. This study has benefited from product sets freely available; we thank these diverse platforms and in particular, SNO SSS and PIRATA. We also thank the TRIATLAS project funded by the European Union's Horizon 2020 research and innovation program under Grant agreement 817578 and the TOSCA SMOS, SWOT-GG, and SWOT-ETAO projects funded by the CNES for their various supports. Computing resources are provided by DARI under Grant GEN7298.

References

- Alory, G., Da-Allada, C. Y., Djakouré, S., Dadou, I., Jouanno, J., & Loemba, D. P. (2021). Coastal upwelling limitation by onshore geostrophic flow in the Gulf of Guinea around the Niger River Plume. *Frontiers in Marine Science*, 7. <https://doi.org/10.3389/fmars.2020.607216>
- Alory, G., Delcroix, T., Téchiné, P., Diverres, D., Varillon, D., Cravatte, S., et al. (2015). The French contribution to the voluntary observing ships network of sea surface salinity. *Deep-Sea Research Part I Oceanographic Research Papers*, 105, 1–18. <https://doi.org/10.1016/j.dsr.2015.08.005>
- Aroucha, L. C., Lübbbecke, J. F., Körner, M., Imbol Koungue, R. A., & Awo, F. M. (2024). The influence of freshwater input on the evolution of the 1995 Benguela Niño. *Journal of Geophysical Research: Oceans*, 129(2). <https://doi.org/10.1029/2023JC020241>
- Awo, F. M., Alory, G., Da-Allada, C. Y., Delcroix, T., Jouanno, J., Kestenare, E., & Baloitcha, E. (2018). Sea surface salinity signature of the tropical Atlantic interannual climatic modes. *Journal of Geophysical Research: Oceans*, 123(10), 7420–7437. <https://doi.org/10.1029/2018JC013837>
- Awo, F. M., Rouault, M., Ostrowski, M., Tomety, F. S., Da-Allada, C. Y., & Jouanno, J. (2022). Seasonal cycle of sea surface salinity in the Angola upwelling system. *Journal of Geophysical Research: Oceans*, 127(7), 1–13. <https://doi.org/10.1029/2022JC018518>

- Bachèlery, M., Illig, S., & Dadou, I. (2016). Interannual variability in the South-East Atlantic Ocean, focusing on the Benguela upwelling system: Remote versus local forcing. *Journal of Geophysical Research: Oceans*, *121*(1), 284–310. <https://doi.org/10.1002/2015JC011168>
- Bentamy, A., & Fillon, D. C. (2012). Gridded surface wind fields from Metop/ASCAT measurements. *International Journal of Remote Sensing*, *33*(6), 1729–1754. <https://doi.org/10.1080/01431161.2011.600348>
- Berit, G. R. (1976). Les eaux froides cotieres du Gabon a L'Angola sont-elles dues a un upwelling d'Ekman, Cah. *ORSTOM Séries Océanographie*, *14*, 273–278.
- Bordbar, M. H., Mohrholz, V., & Schmidt, M. (2021). The relation of wind-driven coastal and offshore upwelling in the Benguela upwelling system. *Journal of Physical Oceanography*, *51*, 3117–3133. <https://doi.org/10.1175/JPO-D-20-0297.1>
- Bourlès, B., Araujo, M., McPhaden, M. J., Brandt, P., Foltz, G. R., Lumpkin, R., et al. (2019). PIRATA: A sustained observing system for tropical Atlantic climate research and forecasting. *Earth and Space Science*, *6*(4), 577–616. <https://doi.org/10.1029/2018EA000428>
- Brandt, P., Alory, G., Awo, F. M., Dengler, M., Djakouré, S., Imbol Koungue, R. A., et al. (2023). Physical processes and biological productivity in the upwelling regions of the tropical Atlantic. *Ocean Science*, *19*(3), 581–601. <https://doi.org/10.5194/os-19-581-2023>
- Brink, K. H. (1982). A comparison of long coastal trapped wave theory with observations off Peru. *Journal of Physical Oceanography*, *12*(8), 897–913. [https://doi.org/10.1175/1520-0485\(1982\)012<0897:ACOLCT>2.0.CO;2](https://doi.org/10.1175/1520-0485(1982)012<0897:ACOLCT>2.0.CO;2)
- Brink, K. H. (2018). Coastal-trapped waves with stratification, topography, mean flow and bottom friction with complex frequency in Matlab [Dataset]. *Woods Hole Open Access Server (WHOAS) at the MBLWHOI Library*. <https://doi.org/10.1575/1912/10525>
- Camara, I., Kolodziejczyk, N., Mignot, J., Lazar, A., & Gaye, A. T. (2015). On the seasonal variations of salinity of the tropical Atlantic mixed layer. *Journal of Geophysical Research: Oceans*, *120*(6), 4441–4462. <https://doi.org/10.1002/2015JC010865>
- Carr, M.-E., & Kearns, E. J. (2003). Production regimes in four eastern boundary current systems. *Deep Sea Research Part II: Topical Studies in Oceanography*, *50*(22–26), 3199–3221. <https://doi.org/10.1016/j.dsr2.2003.07.015>
- Chavez, F. P., & Messié, M. (2009). A comparison of eastern boundary upwelling ecosystems. *Progress in Oceanography*, *83*(1–4), 80–96. <https://doi.org/10.1016/j.pocean.2009.07.032>
- Chin, T. M., Vazquez-Cuervo, J., & Armstrong, E. M. (2017). A multi-scale high-resolution analysis of global sea surface temperature. *Remote Sensing of Environment*, *200*, 154–169. <https://doi.org/10.1016/j.rse.2017.07.029>
- Da-Allada, C. Y., Alory, G., du Penhoat, Y., Jouanno, J., Hounkonnou, M. N., & Kestenare, E. (2014). Causes for the recent increase in sea surface salinity in the North-Eastern Gulf of Guinea. *African Journal of Marine Science*, *36*(2), 197–205. <https://doi.org/10.2989/1814232X.2014.927398>
- de Boyer Montégut, C., Madec, G., Fischer, A. S., Lazar, A., & Iudicone, D. (2004). Mixed layer depth over the global ocean: An examination of profile data and a profile-based climatology. *Journal of Geophysical Research: Oceans*, *109*(C12), 1–20. <https://doi.org/10.1029/2004JC002378>
- Decharme, B., Delire, C., Minvielle, M., Colin, J., Vergnes, J., Alias, A., et al. (2019). Recent changes in the ISBA-CTRIP land surface system for use in the CNRM-CM6 climate model and in global off-line hydrological applications. *Journal of Advances in Modeling Earth Systems*, *11*(5), 1207–1252. <https://doi.org/10.1029/2018ms001545>
- Denamiel, C., Budgell, W. P., & Toumi, R. (2013). The Congo River plume: Impact of the forcing on the far-field and near-field dynamics. *Journal of Geophysical Research: Oceans*, *118*(2), 964–989. <https://doi.org/10.1002/jgrc.20062>
- Dieng, H. B., Dadou, I., Léger, F., Morel, Y., Jouanno, J., Lyard, F., & Allain, D. (2021). Sea level anomalies using altimetry, model and tide gauges along the African coasts in the eastern tropical Atlantic Ocean: Inter-comparison and temporal variability. *Advances in Space Research*, *68*(2), 534–552. <https://doi.org/10.1016/j.asr.2019.10.019>
- Ducet, N., Le Traon, P. Y., & Reverdin, G. (2000). Global high-resolution mapping of ocean circulation from TOPEX/Poseidon and ERS-1 and -2. *Journal of Geophysical Research: Oceans*, *105*(C8), 19477–19498. <https://doi.org/10.1029/2000jc900063>
- Fennel, W., Junker, T., Schmidt, M., & Mohrholz, V. (2012). Response of the Benguela upwelling systems to spatial variations in the wind stress. *Continental Shelf Research*, *45*, 65–77. <https://doi.org/10.1016/j.csr.2012.06.004>
- Foltz, G. R., Grodsky, S. A., Carton, J. A., & McPhaden, M. J. (2003). Seasonal mixed layer heat budget of the tropical Atlantic Ocean. *Journal of Geophysical Research: Oceans*, *108*(C5). <https://doi.org/10.1029/2002JC001584>
- Fore, A. G., Yueh, S. H., Tang, W., Stiles, B. W., & Hayashi, A. K. (2016). Combined active/passive retrievals of ocean vector wind and sea surface salinity with SMAP. *IEEE Transactions on Geoscience and Remote Sensing*, *54*(12), 7396–7404. <https://doi.org/10.1109/TGRS.2016.2601486>
- Fournier, S., Bingham, F. M., González-Haro, C., Hayashi, A., Ulfax Carlin, K. M., Brodnitz, S. K., et al. (2023). Quantification of Aquarius, SMAP, SMOS and ARGO-based gridded sea surface salinity product sampling errors. *Remote Sensing*, *15*(2), 1–16. <https://doi.org/10.3390/rs15020422>
- Gaillard, F., Diverres, D., Jacquin, S., Gouriou, Y., Grelet, J., Le Menn, M., et al. (2015). Sea surface temperature and salinity from French research vessels, 2001–2013. *Scientific Data*, *2*(1), 150054. <https://doi.org/10.1038/sdata.2015.54>
- Garcia, H. E., Boyer, T. P., Baranova, O. K., Locarnini, R. A., Mishonov, A. V., Grodsky, A., et al. (2019). *World Ocean Atlas 2018: Product documentation*. In A. Mishonov (Ed.) (1, pp. 1–20).
- Gutknecht, E., Dadou, I., Le Vu, B., Cambon, G., Sudre, J., Garçon, V., et al. (2013). Coupled physical/biogeochemical modeling including O₂-dependent processes in the eastern boundary upwelling systems: Application in the Benguela. *Biogeosciences*, *10*(6), 3559–3591. <https://doi.org/10.5194/bg-10-3559-2013>
- Herbert, G., & Bourlès, B. (2018). Impact of intraseasonal wind bursts on sea surface temperature variability in the far eastern tropical Atlantic Ocean during boreal spring 2005 and 2006: Focus on the mid-May 2005 event. *Ocean Science*, *14*(4), 849–869. <https://doi.org/10.5194/os-14-849-2018>
- Hopkins, J., Lucas, M., Dufau, C., Sutton, M., Stum, J., Laurent, O., & Channelliere, C. (2013). Detection and variability of the Congo River plume from satellite derived sea surface temperature, salinity, ocean colour and sea level. *Remote Sensing of Environment*, *139*, 365–385. <https://doi.org/10.1016/j.rse.2013.08.015>
- Houndegnonto, O. J., Kolodziejczyk, N., Maes, C., Bourlès, B., Da-Allada, C. Y., & Reul, N. (2021). Seasonal variability of freshwater plumes in the Eastern Gulf of Guinea as inferred from satellite measurements. *Journal of Geophysical Research: Oceans*, *126*(5), 1–27. <https://doi.org/10.1029/2020JC017041>
- Illig, S., & Bachèlery, M. L. (2024). The 2021 Atlantic Niño and Benguela Niño events: External forcings and air–sea interactions. *Climate Dynamics*, *62*(1), 679–702. <https://doi.org/10.1007/s00382-023-06934-0>
- Illig, S., Bachèlery, M. L., & Lübbecke, J. F. (2020). Why do Benguela Niños lead Atlantic Niños? *Journal of Geophysical Research: Oceans*, *125*(9). <https://doi.org/10.1029/2019JC016003>
- Illig, S., Cadier, E., Bachèlery, M., & Kersalé, M. (2018). Subseasonal coastal-trapped wave propagations in the Southeastern Pacific and Atlantic Oceans: I. A new approach to estimate wave amplitude. *Journal of Geophysical Research: Oceans*, *123*(6), 3915–3941. <https://doi.org/10.1029/2017JC013539>

- Illig, S., Dewitte, B., Ayoub, N., du Penhoat, Y., Reverdin, G., De Mey, P., et al. (2004). Interannual long equatorial waves in the tropical Atlantic from a high-resolution ocean general circulation model experiment in 1981–2000. *Journal of Geophysical Research: Oceans*, *109*(C2), C02022. <https://doi.org/10.1029/2003JC001771>
- Jarugula, S., & McPhaden, M. J. (2023). Indian Ocean Dipole affects eastern tropical Atlantic salinity through Congo River Basin hydrology. *Communications Earth & Environment*, *4*(1), 2–10. <https://doi.org/10.1038/s43247-023-01027-6>
- Jouanno, J., Marin, F., Du Penhoat, Y., Sheinbaum, J., & Molines, J. M. (2011). Seasonal heat balance in the upper 100m of the equatorial Atlantic Ocean. *Journal of Geophysical Research: Oceans*, *116*(C9), 1–19. <https://doi.org/10.1029/2010JC006912>
- Kanga, D. K., Kouassi, M. A., Trokourey, A., Toualy, E., N'Guessan, B. K., Brehmer, P., & Ostrowski, M. (2021). Spatial and seasonal variability of mixed layer depth in the tropical Atlantic at 10 W using 40 years of observation data. *European Journal of Scientific Research*.
- Kobayashi, S., Ota, Y., Harada, Y., Ebata, A., Moriya, M., Onoda, H., et al. (2015). The JRA-55 reanalysis: General specifications and basic characteristics. *Journal of the Meteorological Society of Japan*, *93*(1), 5–48. <https://doi.org/10.2151/jmsj.2015-001>
- Körner, M., Brandt, P., & Dengler, M. (2023). Seasonal cycle of sea surface temperature in the tropical Angolan upwelling system. *Ocean Science*, *19*(1), 121–139. <https://doi.org/10.5194/os-19-121-2023>
- Körner, M., Brandt, P., Illig, S., Dengler, M., Subramaniam, A., Bachèlery, M. L., & Krahnmann, G. (2024). Coastal trapped waves and tidal mixing control primary production in the tropical Angolan upwelling system. *Science Advances*, *10*(4), 29–31. <https://doi.org/10.1126/sciadv.adj6686>
- Laraque, A., N'kaya, G. D. M., Orange, D., Tshimanga, R., Tshitenge, J. M., Mahé, G., et al. (2020). Recent budget of hydroclimatology and hydrosedimentology of the Congo River in Central Africa. *Water*, *12*(9), 2613. <https://doi.org/10.3390/w12092613>
- Lellouche, J.-M., Greiner, E., Bourdallé-Badie, R., Garric, G., Melet, A., Drévillon, M., et al. (2021). The Copernicus global 1/12° oceanic and sea ice GLORYS12 reanalysis. *Frontiers of Earth Science*, *9*, 1–27. <https://doi.org/10.3389/feart.2021.698876>
- Le Traon, P. Y., Nadal, F., & Ducet, N. (1998). An improved mapping method of multisatellite altimeter data. *Journal of Atmospheric and Oceanic Technology*, *15*(2), 522–534. [https://doi.org/10.1175/1520-0426\(1998\)015<0522:AIMMOM>2.0.CO;2](https://doi.org/10.1175/1520-0426(1998)015<0522:AIMMOM>2.0.CO;2)
- Lübbecke, J. F., Brandt, P., Dengler, M., Kopte, R., Lüdke, J., Richter, I., et al. (2019). Causes and evolution of the southeastern tropical Atlantic warm event in early 2016. *Climate Dynamics*, *53*(1–2), 261–274. <https://doi.org/10.1007/s00382-018-4582-8>
- Madec, G., Bourdallé-Badie, R., Bouttier, P.-A., Bricaud, C., Bruciaferri, D., Calvert, D., et al. (2017). *NEMO ocean engine*. Notes du Pôle de modélisation de l'Institut Pierre-Simon Laplace (IPSL), Vol. 27, 1288–1619. <https://doi.org/10.5281/zenodo.3248739>
- Martins, M. S., & Stammer, D. (2022). Interannual variability of the Congo River plume-induced sea surface salinity. *Remote Sensing*, *14*(4), 1013. <https://doi.org/10.3390/rs14041013>
- Materia, S., Gualdi, S., Navarra, A., & Terray, L. (2012). The effect of Congo River freshwater discharge on eastern equatorial Atlantic climate variability. *Climate Dynamics*, *39*(9–10), 2109–2125. <https://doi.org/10.1007/s00382-012-1514-x>
- Murtugudde, R., Beauchamp, J., McClain, C. R., Lewis, M., & Busalacchi, A. J. (2002). Effects of penetrative radiation of the upper tropical ocean circulation. *Journal of Climate*, *15*(5), 470–486. [https://doi.org/10.1175/1520-0442\(2002\)015<0470:EOPROT>2.0.CO;2](https://doi.org/10.1175/1520-0442(2002)015<0470:EOPROT>2.0.CO;2)
- Ngakala, R. D., Alory, G., Da-Allada, C. Y., Kom, O. E., Jouanno, J., Rath, W., & Baloitcha, E. (2023). Joint observation-model mixed-layer heat and salt budgets in the eastern tropical Atlantic. *Ocean Science*, *19*(3), 535–558. <https://doi.org/10.5194/os-19-535-2023>
- Okumura, Y., & Xie, S.-P. (2006). Some overlooked features of tropical Atlantic climate leading to a new Niño-like Phenomenon. *Journal of Climate*, *19*(22), 5859–5874. <https://doi.org/10.1175/JCLI3928.1>
- Ostrowski, M., Da Silva, J. C. B., & Bazik-Sangolay, B. (2009). The response of sound scatterers to El Niño- and La Niña-like oceanographic regimes in the southeastern Atlantic. *ICES Journal of Marine Science*, *66*(6), 1063–1072. <https://doi.org/10.1093/icesjms/fsp102>
- Peter, A. C., Le Hénaff, M., du Penhoat, Y., Menkes, C. E., Marin, F., Vialard, J., et al. (2006). A model study of the seasonal mixed layer heat budget in the equatorial Atlantic. *Journal of Geophysical Research: Oceans*, *111*(C6), 1–16. <https://doi.org/10.1029/2005JC003157>
- Pham, H. T., & Sarkar, S. (2018). Ageostrophic secondary circulation at a submesoscale front and the formation of gravity currents. *Journal of Physical Oceanography*, *48*(10), 2507–2529. <https://doi.org/10.1175/JPO-D-17-0271.1>
- Picaut, J. (1983). Propagation of the seasonal upwelling in the eastern equatorial Atlantic. *Journal of Physical Oceanography*, *13*(1), 18–37. [https://doi.org/10.1175/1520-0485\(1983\)013<0018:potsui>2.0.co;2](https://doi.org/10.1175/1520-0485(1983)013<0018:potsui>2.0.co;2)
- Piton, B. (1988). Les courants sur le plateau continental devant Pointe-Noire (Congo). *Documents scientifiques. ORSTOM*, *37*.
- Rouault, M., Servain, J., Reason, C. J. C., Bourlès, B., Rouault, M. J., & Fauchereau, N. (2009). Extension of PIRATA in the tropical South-East Atlantic: An initial one-year experiment. *African Journal of Marine Science*, *31*(1), 63–71. <https://doi.org/10.2989/ajms.2009.31.1.5.776>
- Scannell, H. A., & McPhaden, M. J. (2018). Seasonal mixed layer temperature balance in the southeastern tropical Atlantic. *Journal of Geophysical Research: Oceans*, *123*(8), 5557–5570. <https://doi.org/10.1029/2018JC014099>
- Topé, G. D. A., Alory, G., Djakouré, S., Da-Allada, C. Y., Jouanno, J., & Morvan, G. (2023). How does the Niger River warm coastal waters in the Northern Gulf of Guinea? *Frontiers in Marine Science*, *10*, 1–11. <https://doi.org/10.3389/fmars.2023.1187202>
- Umlauf, L., & Burchard, H. (2003). A generic length-scale equation for geophysical turbulence models. *Journal of Marine Research*, *61*(2), 235–265. <https://doi.org/10.1357/002224003322005087>
- Umlauf, L., & Burchard, H. (2005). Second-order turbulence closure models for geophysical boundary layers. A review of recent work. *Continental Shelf Research*, *25*(7–8), 795–827. <https://doi.org/10.1016/j.csr.2004.08.004>
- Vallaes, V., Lambrechts, J., Delandmeter, P., Pätsch, J., Spitz, A., Hanert, E., & Deleersnijder, E. (2021). Understanding the circulation in the deep, micro-tidal and strongly stratified Congo River Estuary. *Ocean Modelling*, *167*, 101890. <https://doi.org/10.1016/j.ocemod.2021.101890>
- Vic, C., Berger, H., Tréguier, A. M., & Couvelard, X. (2014). Dynamics of an equatorial river plume: Theory and numerical experiments applied to the Congo plume case. *Journal of Physical Oceanography*, *44*(3), 980–994. <https://doi.org/10.1175/JPO-D-13-0132.1>
- Voituriez, B., & Herbland, A. (1982). Comparaison des systèmes productifs de l'Atlantique tropical Est: Dômes thermiques, upwellings côtiers et upwelling équatorial, Rapp. Procès-Verbaux des Réunion Cons. *Int. pour l'Exploration la Mer*, *180*, 114–130.
- Wacongne, S., & Piton, B. (1992). The near-surface circulation in the Northeastern Corner of the South Atlantic Ocean. *Deep Sea Research Part A. Oceanographic Research Papers*, *39*(7–8), 1273–1298. [https://doi.org/10.1016/0198-0149\(92\)90069-6](https://doi.org/10.1016/0198-0149(92)90069-6)
- Wade, M., Caniaux, G., & Du Penhoat, Y. (2011). Variability of the mixed layer heat budget in the eastern equatorial Atlantic during 2005–2007 as inferred using Argo floats. *Journal of Geophysical Research: Oceans*, *116*(C8), 1–17. <https://doi.org/10.1029/2010JC006683>
- White, R. H., & Toumi, R. (2014). River flow and ocean temperatures: The Congo River. *Journal of Geophysical Research: Oceans*, *119*(4), 2501–2517. <https://doi.org/10.1002/2014JC009836>
- Zeng, Z., Brandt, P., Lamb, K. G., Greatbatch, R. J., Dengler, M., Claus, M., & Chen, X. (2021). Three-dimensional numerical simulations of internal tides in the Angolan upwelling region. *Journal of Geophysical Research: Oceans*, *126*(2), 1–20. <https://doi.org/10.1029/2020JC016460>